

# Modelling of diesel spray flames under engine-like conditions using an accelerated Eulerian Stochastic Fields method

Pang, Kar Mun; Jangi, Mehdi; Bai, Xue Song; Schramm, Jesper; Walther, Jens Honore

DOI:

[10.1016/j.combustflame.2018.03.030](https://doi.org/10.1016/j.combustflame.2018.03.030)

License:

Creative Commons: Attribution-NonCommercial-NoDerivs (CC BY-NC-ND)

*Document Version*

Peer reviewed version

*Citation for published version (Harvard):*

Pang, KM, Jangi, M, Bai, XS, Schramm, J & Walther, JH 2018, 'Modelling of diesel spray flames under engine-like conditions using an accelerated Eulerian Stochastic Fields method', *Combustion and Flame*, vol. 193, pp. 363-383. <https://doi.org/10.1016/j.combustflame.2018.03.030>

[Link to publication on Research at Birmingham portal](#)

## General rights

Unless a licence is specified above, all rights (including copyright and moral rights) in this document are retained by the authors and/or the copyright holders. The express permission of the copyright holder must be obtained for any use of this material other than for purposes permitted by law.

- Users may freely distribute the URL that is used to identify this publication.
- Users may download and/or print one copy of the publication from the University of Birmingham research portal for the purpose of private study or non-commercial research.
- User may use extracts from the document in line with the concept of 'fair dealing' under the Copyright, Designs and Patents Act 1988 (?)
- Users may not further distribute the material nor use it for the purposes of commercial gain.

Where a licence is displayed above, please note the terms and conditions of the licence govern your use of this document.

When citing, please reference the published version.

## Take down policy

While the University of Birmingham exercises care and attention in making items available there are rare occasions when an item has been uploaded in error or has been deemed to be commercially or otherwise sensitive.

If you believe that this is the case for this document, please contact [UBIRA@lists.bham.ac.uk](mailto:UBIRA@lists.bham.ac.uk) providing details and we will remove access to the work immediately and investigate.

# Modelling of diesel spray flames under engine-like conditions using an accelerated Eulerian Stochastic Fields method

Kar Mun Pang<sup>\*,a</sup>, Mehdi Jangi<sup>b</sup>, Xue-Song Bai<sup>c</sup>, Jesper Schramm<sup>a</sup>, Jens Honore Walther<sup>a,d</sup>

<sup>a</sup> Department of Mechanical Engineering, Technical University of Denmark, 2800 Kgs. Lyngby, Denmark

<sup>b</sup> Department of Mechanical Engineering, University of Birmingham, B15 2TT Birmingham, The United Kingdom

<sup>c</sup> Department of Energy Sciences, Lund University, 22100 Lund, Sweden

<sup>d</sup> Computational Science and Engineering Laboratory, ETH Zürich, CH-8092 Zürich, Switzerland

\*Corresponding author's email: [kmpan@mek.dtu.dk](mailto:kmpan@mek.dtu.dk)

## Abstract

This paper aims to simulate diesel spray flames across a wide range of engine-like conditions using the Eulerian Stochastic Field probability density function (ESF-PDF) model. The ESF model is coupled with the Chemistry Coordinate Mapping approach to expedite the calculation. A convergence study is carried out for a number of stochastic fields at five different conditions, covering both conventional diesel combustion and low-temperature combustion regimes. Ignition delay time, flame lift-off length as well as distributions of temperature and various combustion products are used to evaluate the performance of the model. The peak values of these properties generated using thirty-two stochastic fields are found to converge, with a maximum relative difference of 27% as compared to those from a greater number of stochastic fields. The ESF-PDF model with thirty-two stochastic fields performs reasonably well in reproducing the experimental

1 flame development, ignition delay times and lift-off lengths. The ESF-PDF model also predicts a  
2 broader hydroxyl radical distribution which resembles the experimental observation, indicating that  
3 the turbulence-chemistry interaction is captured by the ESF-PDF model. The validated model is  
4 subsequently used to investigate the flame structures under different conditions. Analyses based on  
5 flame index and formaldehyde distribution suggest that a triple flame, which consists of a rich  
6 premixed flame, a diffusion flame and a lean premixed flame, is established in the earlier stage of the  
7 combustion. As the combustion progresses, the lean premixed flame weakens and diminishes with  
8 time. Eventually, only a double-flame structure, made up of the diffusion flame and the rich  
9 premixed flame, is observed. The analyses for various ambient temperatures show that the triple-  
10 flame structure remains for a longer period of time in cases with lower ambient temperatures. The  
11 present study shows that the ESF-PDF method is a valuable alternative to Lagrangian particle PDF  
12 methods.

13  
14  
15  
16  
17  
18  
19  
20  
21  
22  
23  
24  
25  
26  
27  
28  
29  
30  
31 **Keywords:** diesel engine, Eulerian Stochastic Fields, probability density function, spray flame,  
32 turbulent combustion  
33

## 34 35 36 37 38 39 **1. Introduction**

40  
41 To comply with the increasingly stringent regulations that aim to reduce emitted harmful pollutants  
42 from diesel engines, the implementation of alternative fuels and new engine combustion technologies  
43 such as low-temperature combustion (LTC) has become the main focus of both the automotive and  
44 maritime engine industries. With the use of alternative fuel and/or LTC, the associated combustion  
45 modes are expected to be different from that of conventional diesel combustion in the same operating  
46 strategy, which may be varying from a classical diffusion-controlled combustion to a partially  
47 premixed reacting system where ignition, premixed reaction front and diffusion flame can co-exist  
48 and interact with each other [1]. It is necessary to couple advanced experimental and numerical tools

1 for the investigation and understanding of the auto-ignition, flame stabilisation/propagation and  
2 emissions formation. The experimentation using laser diagnostics and high-speed photography  
3 incorporated with optically accessible combustion chambers [2-8] and engines [9] is a promising  
4 approach to provide a more comprehensive understanding of in-cylinder phenomena. The optical  
5 measurements also serve as an important asset for validating newly developed turbulent combustion  
6 models. These models, once validated, can arguably provide a qualitative picture of the missing data  
7 and be used to infer characteristics of flame structures that cannot yet be measured [10]. The  
8 validated model can also be used to simulate and elucidate in-cylinder events of engines which are  
9 not optically accessible, expanding on the limited details from experimental exhaust measurements  
10 in a more cost-effective manner [11,12].  
11  
12  
13  
14  
15  
16  
17  
18  
19  
20  
21  
22  
23

24 With the aim to achieve more accurate predictions of combustion and emissions formation  
25 processes, it is now widely accepted that a more comprehensive chemistry should be incorporated  
26 into multi-dimensional computational fluid dynamics (CFD) studies [13], instead of semi-global or  
27 global reaction mechanisms. In particular, the presence of low-temperature chemistry is essential to  
28 simulate the first stage (cool-flame) ignition [14] since the cool flame behaviour may then influence  
29 the second stage (high-temperature) ignition. Also, radicals such as oxygen atom (O) and hydroxyl  
30 (OH) should be present since they are pertinent species for the formation of nitric oxides (NO<sub>x</sub>) [15]  
31 and sulphur oxides (SO<sub>x</sub>) [16]. For detailed soot modelling, reactions of aromatics and Polycyclic  
32 Aromatic Hydrocarbon (PAH) are required [17]. Otherwise, for semi-empirical soot models,  
33 acetylene (C<sub>2</sub>H<sub>2</sub>) has to be taken into account in the combustion chemistry [18]. Prior to  
34 implementing a combustion chemistry with CFD codes, a common practice is to validate the reaction  
35 pathways and the associated rate constants under conditions of interest using measurements obtained  
36 from shock tube, plug flow and flame speed experiments.  
37  
38  
39  
40  
41  
42  
43  
44  
45  
46  
47  
48  
49  
50  
51  
52  
53  
54  
55  
56  
57  
58  
59  
60  
61  
62  
63  
64  
65

Table 1. Numerical studies on the ECN sprays performed in year 2013 to 2016.

Investigator(s)	Framework	Type of fuel combustion	TCI closure	Soot model
Jangi et al. [1]	URANS	<i>n</i> -Heptane	ESF	-
Pei et al. [10,21]	URANS	<i>n</i> -Dodecane	L-tPDF	-
Pang et al. [12, 29,43]	URANS	Diesel, <i>n</i> -Heptane	WSR	Four-step
D’Errico et al. [13]	URANS	<i>n</i> -Dodecane	WSR+PDF	-
Pei et al. [19,20]	URANS	<i>n</i> -Heptane	L-tPDF	-
Bhattacharjee and Haworth [22]	URANS	<i>n</i> -Heptane, <i>n</i> -Dodecane	L-tPDF	-
Bolla et al. [23-25]	URANS	<i>n</i> -Heptane, Diesel	CMC	Four-step
Irannejad et al. [27]	LES	<i>n</i> -Heptane	FMDF	-
Lucchini et al. [28]	URANS	<i>n</i> -Dodecane	ESF	-
Wang et al. [30]	URANS	<i>n</i> -Dodecane	WSR	Five-step
Gong et al. [31]	LES	<i>n</i> -Dodecane	WSR	Two-step
Chishty et al. [32]	URANS	<i>n</i> -Dodecane	L-tPDF	Four-step
Frassoldati et al. [33]	URANS	<i>n</i> -Dodecane	mRIF	-
Cheng et al. [34]	URANS	Biodiesel	WSR	Four-step
Poon et al. [35]	URANS	Diesel	WSR	Four-step
Vishwanathan and Reitz [36]	URANS	Diesel	WSR	Five-step
D’Errico et al. [37]	URANS	<i>n</i> -Dodecane	WSR, mRIF	-
Gong et al. [38]	URANS	<i>n</i> -Heptane	ESF	-
Gallot-Lavallée and Jones [39]	LES	<i>n</i> -Heptane	ESF	-
Pandurangi et al. [40]	URANS	<i>n</i> -Dodecane	CMC	Four-step
Wehrfritz et al. [41]	LES	<i>n</i> -Dodecane	FGM	-
Jangi et al. [42]	URANS	<i>n</i> -Heptane	WSR	Two-step
Bolla et al. [44,45]	URANS	<i>n</i> -Dodecane	L-tPDF	Four-step

Note: L-tPDF denotes the Lagrangian particle transported PDF model. The two-step soot model represents the Hiroyasu-Nagle and Strickland-Constable (NSC) model which describes soot formation and oxidation [48]. The four-step soot model denotes that developed by Leung et al. [18] where soot nucleation, surface growth, coagulation and oxidation are accounted for. The five-step model considers PAH condensation on top of the four-step soot model [36].

In addition to the validated combustion chemistry, turbulence-chemistry interaction (TCI) closure strategies become an important subject and various numerical studies have proven that TCI affects the computation of ignition delay time, lift-off length and reacting zone thickness [19-24]. Furthermore, an advanced turbulent combustion model should also have the capability to capture multiple combustion modes, which may occur in the engines as aforementioned [1,10,26]. Numerous TCI closure approaches have been developed for the modelling of turbulent spray combustion under engine relevant conditions. The coupling of TCI closure approaches and chemical kinetic models is often validated using the data provided by Engine Combustion Network (ECN) [2]. Modelling of the ECN spray flames have been performed in both the unsteady Reynolds-averaged Navier–Stokes (URANS) and Large Eddy Simulation (LES) frameworks. Detailed summaries of these works until year 2013 can be found in Refs. [19,22] and the references therein. The research is currently being pursued in multiple streams, including focuses on chemical kinetics, TCI effects and the combustion

physics. Those performed in 2013 and onwards are summarised in Table 1. The commonly used TCI closure approaches include Flamelet Generation Manifold (FGM), multiple Representative Interaction Flamelet (mRIF), Conditional Moment-Closure (CMC) and probability density function (PDF). The ‘simplest TCI closure’ has also been frequently used, *i.e.* the mean chemical source term is directly evaluated using the mean temperature and composition neglecting turbulent fluctuations. In the literature, this approach is referred by different names, for example, direct integration, perfectly-stirred reactor or well-stirred reactor (WSR). This type of model will henceforth be addressed as WSR in this article. In order to simulate the multiple combustion modes, D’Errico et al. [37] proposed to combine different models, *i.e.* WSR and PDF.

The conventional CMC method has been successfully applied to various non-premixed combustion in the past; however, its application to premixed flames remained a challenge, due to the modelling of the progress variable [26,46]. An algebraic model was proposed by Azmin et al. [46] to address this limitation and the results suggested that the CMC, which considered a second conditioning variable, may be applied across the regimes of premixed combustion. However, this is yet to be validated in spray flame simulations. Alternatively, Wright et al. [26] implemented a fully elliptic first-order CMC model for spray autoignition simulations under diesel engine-like conditions. De Paola et al. [47] also employed the same method for diesel engine simulations. Their works showed that the single model can predict the autoignition, diffusion flame mode as well as certain features of the premixed mode such as flame propagations in the spray combustion [26]. The CMC model was also used to simulate *n*-heptane and diesel fuel spray combustion in the Sandia combustion chamber [23-25,40].

The transported PDF method is a more sophisticated TCI closure approach that solves the transport equation for the one-point, one-time Eulerian joint PDF of velocity and composition or alternatively composition only. The main advantage of the transported PDF method, as compared to the previous TCI closure strategies, is that no closure problems arising from averaging of one-point

non-linear chemical reaction rate terms in the governing equations. The transported PDF method has the largest validity range and a single model to be used for computation of the auto-ignition and different levels of “premixedness”, *i.e.* premixed, partially premixed and non-premixed [1,10]. Pei et al. [10,19-21] have used the Lagrangian particle transported PDF (L-tPDF) in ANSYS FLUENT to simulate spray combustion of *n*-heptane and *n*-dodecane across a wide range of thermochemical conditions as well as injection parameters. Bolla et al. [44,45] used the same approach to study the effects of multiple injection and turbulence-chemistry-radiation interaction. In their studies, Lagrangian particle tracking method could not be used together with the L-tPDF method and a “gas-jet” approach was used to simulate the fuel spray event. In a separate work performed by Bhattacharjee and Haworth [22], a stochastic Lagrangian parcel fuel-injector and spray model formulation (based on a droplet distribution function method) was coupled with a transported PDF method (using a separate stochastic Lagrangian particle method) to simulate transient auto-ignition and combustion in turbulent spray flames of *n*-heptane and *n*-dodecane.

The transported PDF model can also be formulated in the Eulerian framework [50,51]. The Eulerian PDF is also known as Eulerian Stochastic Fields (ESF) model. When the same chemical mechanism and the same micro-mixing model were used, both ESF model and its Lagrangian counterpart generated similar results [51]. The principal motivation for ESF compared to Lagrangian-based PDF is the relative ease of implementation of the former into CFD codes [22,50]. One of the first efforts to implement the ESF model with URANS for diesel spray combustion was performed by Lucchini et al. [28]. However, their numerical work only focused on the early stage of combustion. More recently, Jangi et al. [1] used the ESF model to investigate the effects of fuel octane number on ignition, lift-off and combustion of the spray flames. Besides that, Gong et al. [38] used the ESF method to study the diesel flame lift-off stabilisation in the presence of laser-ignition. In these studies, the Chemistry Coordinate Mapping (CCM) method was coupled with the ESF solver in order to expedite the calculation. The coupled model is henceforth addressed as the ESF-

CCM model for brevity. Comparison to experimental measurements showed that the ESF-CCM approach is able to better reproduce the lift-off lengths as compared to those of WSR. This observation agrees with other numerical works [1]. Yet, in the works of Jangi et al. [1] and Gong et al. [38], only a single condition was used for validation in their respective study. In other words, the validity of the ESF-CCM solver in simulating diesel flame across a wide range of engine conditions has yet to be assessed, particularly those closer to the LTC regime. Also, only a semi-global primary reference fuel mechanism was incorporated with the ESF-CCM solver. Important flame indicator species such as formaldehyde ( $\text{CH}_2\text{O}$ ) and OH were absent, which prohibited a detailed analysis on the simulated turbulent spray flames.

Set against these backgrounds, the main objectives of this work are two-fold. Firstly, the validity of the coupling of the ESF-CCM solver and different chemical kinetic mechanisms is assessed in the URANS framework. The operating conditions are extended from conventional diesel combustion regime to LTC regime. The tested conditions also cover a higher ambient density (or pressure) level. Validation is carried out using experimental data from an optically accessible, constant volume combustion chamber as well as a conceptual model inferred by these measurements [2-8]. Secondly, upon validation of the turbulent combustion model, detailed spray flame structures under several targeted conditions are investigated to improve the understanding of the combustion process in various conditions.

The remainder of the paper is structured as follows. First, the test cases are described to provide information about the target spray flame conditions. This is then followed by the descriptions of the numerical formulation, with an emphasis on the ESF-CCM model. The subsequent sections report on detailed sensitivity study and model validation based on optical measurements. This is followed by the analyses of flame structures. Concluding remarks from this work are then highlighted in the final section.

## 2. Case descriptions

Operating conditions and the corresponding injection characteristics considered in the current simulations are summarised in Table 2. As can be seen, two non-reacting spray cases (cases 1 and 2) are used for the validation of spray breakup and turbulence models. The initial ambient ( $T_{am}$ ) temperature is set to 900 K while the initial pressure is adjusted to produce the initial gas density of 22.8 kg/m<sup>3</sup>. Reacting spray cases with an ambient O<sub>2</sub> level of 15% by mole fraction (cases 3 and 4) under the same ambient temperature and density are next simulated. These are the ECN Spray A conditions which are widely studied [4]. Many different fuels have been investigated under this condition [4,6-8]. Here, both the *n*-dodecane (C<sub>12</sub>) and the conventional grade two diesel fuel (D2) experimental data are used [4,6-8]. The initial temperature is also increased to 1000 K to evaluate the model performance in predicting the effects of temperature on the quasi-steady combustion and soot characteristics (cases 5 and 6). The numerical model is also further validated using D2 experimental data collected across a wider range of ambient temperature from 800 to 1100 K at a fixed ambient density of 14.8 kg/m<sup>3</sup> for both O<sub>2</sub> levels of 15% and 21%. The temperature sweep is performed to emulate the in-cylinder engine condition when different injection timings are used while the 15% and 21% O<sub>2</sub> levels are used to imitate the conditions with and without exhaust gas recirculation (EGR) respectively. For the 21% O<sub>2</sub> condition, the ambient density is increased from 14.8 to 30.0 kg/m<sup>3</sup>. Within the tested ambient temperature range, the simulated conditions correspond to ambient pressures of 35 to 95 bar, which cover the thermochemical conditions in practical light duty diesel engine, heavy duty diesel engine and marine engine [11,12]. The experimental ignition delay time and lift-off length measurements are collected from the ECN database [2] and descriptions of these test cases can be found in Ref. [3]. For the simulation results, the ignition delay time is defined as the time when the greatest pressure rise is observed, while the lift-off length is defined as the axial distance from the nozzle at which the computed Favre-averaged mean OH mass fraction reaches a

value that is 2% of its maximum value for the corresponding operating condition. These definitions correspond to those suggested by the ECN.

Table 2. Operating conditions and injection characteristics in the current simulations.

Case	$\rho_{am}$ (kg/m <sup>3</sup> )	$T_{am}$ (K)	[O <sub>2</sub> ] by mole fraction	Fuel type (-)	$T_f$ (K)	$P_{inj}$ (bar)	$D_{nozz}$ ( $\mu$ m)	Refs.
1	22.8	900	0%	C <sub>12</sub>	373	1500	90	[4]
2	22.8	900	0%	D2	373	1500	90	[6]
3	22.8	900	15%	C <sub>12</sub>	373	1500	90	[4]
4	22.8	900	15%	D2	373	1500	90	[6,7]
5	22.8	1000	15%	C <sub>12</sub>	373	1500	90	[4]
6	22.8	1000	15%	D2	373	1500	90	[6,7]
7	14.8	800	15%	D2	436	1400	100	[3]
8	14.8	900	15%	D2	436	1400	100	[3]
9	14.8	1000	15%	D2	436	1400	100	[3]
10	14.8	1100	15%	D2	436	1400	100	[3]
11	14.8	800	21%	D2	436	1400	100	[3]
12	14.8	850	21%	D2	436	1400	100	[3]
13	14.8	900	21%	D2	436	1400	100	[3]
14	14.8	950	21%	D2	436	1400	100	[3]
15	14.8	1000	21%	D2	436	1400	100	[3]
16	14.8	1100	21%	D2	436	1400	100	[3]
17	30.0	800	21%	D2	436	1400	100	[3]
18	30.0	850	21%	D2	436	1400	100	[3]
19	30.0	900	21%	D2	436	1400	100	[3]
20	30.0	950	21%	D2	436	1400	100	[3]
21	30.0	1000	21%	D2	436	1400	100	[3]
22	30.0	1100	21%	D2	436	1400	100	[3]

Note: Operating conditions and injection characteristics of cases 7 to 22 can be obtained in the ECN website [2] while detailed descriptions of the experiments can be found in [3].

### 3. Numerical methods

The multi-dimensional CFD spray combustion simulations are carried out using the open-source code, OpenFOAM version 3.0.1 [52]. In the present study, the URANS is used to model the turbulent flow. The fuel spray, flow and combustion processes are modelled using the Lagrangian-Eulerian approach.

#### 3.1 Spray modelling

The liquid phase of the fuels is modelled with discrete parcels whose motion is described using the Lagrangian particle tracking approach. Each parcel represents a group of spherical droplets whose

position, size, and physical properties are similar. In this work, the Reitz-Diwakar model is used to simulate the fuel droplet breakup, where the stripping breakup model constant,  $C_s$  is adjusted to 11 and 14 to replicate the experimental liquid length penetration of  $n$ -dodecane and D2 fuels respectively. The liquid properties of  $C_{14}H_{30}$  are used to represent that of D2 fuel [53]. Gas and liquid phases are coupled through the mass, momentum, and heat-exchange source terms between the phases. The Frossling model and the Ranz-Marshall correlation are employed to calculate the droplet evaporation and heat transfer with the surrounding gas phase respectively.

### 3.2 Unsteady Reynolds-averaged Navier–Stokes

The gas phase is described in the Eulerian framework using the URANS equations. Due to the ensemble average in the URANS approach, several unclosed terms appear in the governing equations of momentum, species and enthalpy. The eddy viscosity (or the so-called gradient transport) model is used, in which the transports due to the turbulent fluctuation are modelled based on the gradients of mean quantities. Akin to that reported by Christy et al. [32] and Bolla et al. [44,45] in their non-reacting  $n$ -dodecane spray case (case 1), the Realisable  $k$ - $\varepsilon$  model is employed for the turbulence modelling. The initial turbulent kinetic energy,  $k$  and the associated dissipation rate,  $\varepsilon$  are set to  $0.735 \text{ m}^2/\text{s}^2$  and  $0.567 \text{ m}^2/\text{s}^3$  respectively [29]. As can be seen in Fig. 1, the penetration lengths in both  $n$ -dodecane and D2 spray cases as well as the mixture fraction in the  $n$ -dodecane spray case are reasonably well estimated by the model. For the reacting spray simulations, a well-known unclosed term in the mean transport equations is the mean chemical reaction rate. The closure of this term requires a TCI closure approach. In this work, the ESF method, which is presented in the next subsection, is used to couple with the URANS approach [1,38,50].

### 3.2.1 Eulerian Stochastic Field

The ESF-PDF model used here was developed by Valino [50], a detailed description can be found therein. The model has been applied to simulate various combustion problems [1,51,54]. In the ESF method, the turbulent reactive flows are represented by  $n_{sf}$  stochastic fields for each of the  $n_s$  scalars, namely  $\phi_\alpha^{(n)}(x,t)$  for  $1 \leq n \leq n_{sf}$ ,  $1 \leq \alpha \leq n_s$ . In this way, the joint PDF,  $P(\phi; x, t)$ , is represented by an ensemble of the stochastic fields,

$$P(\phi; x, t) = \frac{1}{n_{sf}} \sum_{n=1}^{n_{sf}} \prod_{\alpha=1}^{n_s} \delta(\phi_\alpha - \phi_\alpha^{(n)}) \quad (1)$$

where  $\delta$  is the Dirac delta function. The governing equation for the  $n$ -th stochastic field is

$$\begin{aligned} \overline{\rho} d\phi_\alpha^{(n)} = & -\overline{\rho} u_i \frac{\partial \phi_\alpha^{(n)}}{\partial x_i} dt + \overline{\rho} S_\alpha^r(\phi^{(n)}) dt + \overline{\rho} S_\alpha^s(\phi^{(n)}) dt \\ & + \frac{\partial}{\partial x_i} \left( \Gamma_t \frac{\partial \phi_\alpha^{(n)}}{\partial x_i} \right) dt - \frac{1}{2} \overline{\rho} C_\phi (\phi_\alpha^{(n)} - \phi_\alpha) \omega_t dt + \overline{\rho} \sqrt{\frac{\Gamma_t}{\rho}} \left( \frac{\partial \phi_\alpha^{(n)}}{\partial x_i} \right) dW_i^{(n)} \end{aligned} \quad (2)$$

where  $\phi_\alpha$  denotes the mass fraction of species ( $Y_i$ ) or the enthalpy of the mixture ( $h$ ), and

$\phi^{(n)} = [Y_1^{(n)}, Y_2^{(n)}, \dots, Y_i^{(n)}, h^{(n)}]$ . The first term on the right hand side (r.h.s.) represents the convective term while the second term,  $\overline{\rho} S_\alpha^r(\phi^{(n)}) dt$ , is due to the chemical reactions. The third term,  $\overline{\rho} S_\alpha^s(\phi^{(n)}) dt$  is the source term due to the spray evaporation. This is different for each specie, *i.e.* solely the evaporating specie is involved but it is identical for each stochastic field. The fourth term corresponds to a gradient transport model for turbulent velocity fluctuation, where  $\Gamma_t = \mu_t / \sigma_t$  is the turbulent diffusivity. Here,  $\mu_t$  is the turbulent viscosity while  $\sigma_t$  is the turbulent Schmidt number ( $Sc_t$ ) in the transport equations for chemical species or the Prandtl number ( $Pr_t$ ) in the enthalpy transport equation. Both  $Sc_t$  and  $Pr_t$  are set to 0.7 in the current work. The fifth term, which involves the mixing constant,  $C_\phi$ , represents the molecular mixing. It is modelled using the Interaction with Exchange to the Mean (IEM) model.  $\omega_t$  therein is the turbulence frequency obtained

from  $\omega_t = \varepsilon / k$  where  $k$  and  $\varepsilon$  being the turbulent kinetic energy and its dissipation rate. In the last term on the r.h.s.,  $dW^{(n)}$  represents a vector Wiener process that is spatially uniform but different for each field. The purpose of this term is to introduce a stochastic noise in the transport equations and generate consequent PDF for chemical species and enthalpy. In these simulations,  $dW^{(n)}$  is represented by a time-step increment  $\Delta t^{1/2} \eta_i^n$ , where  $\eta_i^n = \{-1, 1\}$  is a dichotomic random vector. The mean and the moments of each variable can be approximated from the ensemble of  $n_{sf}$  stochastic fields. For example, the mean is

$$\phi_\alpha = \frac{1}{n_{sf}} \sum_{n=1}^{n_{sf}} \phi_\alpha^{(n)} \quad (3)$$

### 3.2.2 Chemistry Coordinate Mapping approach

One of the main limitations of the transported PDF method is its high computational cost. The CCM approach, which was developed by Jangi and Bai [55], is used to expedite the calculation. It has previously been coupled with the L-tPDF model for the URANS simulation of a non-premixed methane/air jet flame [56]. The CCM approach has also been used together with the ESF method in URANS for diesel spray simulations [1,38] as well as in LES for the simulations of bluff body flames [57] and pool fires [58]. In the case of URANS simulations of diesel spray, the implementation of the CCM method with the ESF model showed that a speedup factor of approximately 25 can be achieved when the spray flame during quasi-steady state [1].

The basic idea of the CCM method is to map the reactive composition vector,  $\phi(x, t)$ , from the physical space, to a reduced-dimensional composition space using a clustering technique [59] or sometimes is referred as a cell-agglomeration [60] technique. Coupling of the ESF and CCM models is the same as that reported by Jangi et al. [1]. In principle, the CCM phase space consists of a subset of the composition space. The mapping of the  $n$ -th field with composition

$\phi^{(n)} = [Y_1^{(n)}, Y_2^{(n)}, \dots, Y_i^{(n)}, h^{(n)}]$  into the discretised phase space can be considered as a mapping between the CFD cell index  $(i, j, k)$  in the  $n$ -th field to the zone index in the discretised phase space. The  $(i, j, k)$  CFD cell at time  $t$  in the  $n$ -th field is mapped to the  $l$ -th zone in direction  $\alpha$  of the phase space according to

$$q_\alpha^{(n)}(i, j, k, t) = l, \text{ if } \zeta_\alpha(l) \leq \phi_\alpha^{(n)}(i, j, k, t) < \zeta_\alpha(l) + \Delta\zeta_\alpha \quad (\alpha = 1, 2, \dots, n_s + 1) \quad (4)$$

$$\zeta_\alpha(l) = \zeta_\alpha^{\min}(t_n) + (l-1)\Delta\zeta_\alpha \quad (5)$$

$\zeta_\alpha(l)$ , shown in Eq. (5), is the coordinate of the phase space and  $\Delta\zeta_\alpha$  is the resolution in the discretised phase space.  $\zeta_\alpha^{\min}(t_n)$  is the minimum value of  $\phi_\alpha$  of the overall notional fields at time  $t_n$ . Each zone in the phase space corresponds typically to multiple cells in the notional fields. An integer zone index,  $Z_{id}$ , as described by Eq. (6), is assigned to each notional field such that each zone index denotes one point in the discretised phase space.

$$Z_{id}^{(n)}(i, j, k, t) = \sum_{\alpha=1}^{n_s+1} \prod_{r=1}^{\alpha-1} N_r q_\alpha^{(n)}(i, j, k, t) \quad (6)$$

Here,  $N_r$  is the total number of zones in  $\zeta_r$ . This zone index facilitates storing mapping cells into a one-dimensional array, instead of a multidimensional Cartesian phase space. Through this approach, the memory required for the CCM will be significantly reduced since the memory is only allocated to the zones that contain at least one cell of the notional fields; this zone type is hereinafter referred as the ‘active zone’. The mass-averaged value of  $\phi_\alpha$  in the active zones of the phase space (denoted by

$\hat{\phi}_\alpha$ ) is calculated following the mapping

$$\hat{\phi}_\alpha^{(n)}(\eta_1, \eta_2, \dots, \eta_{n_s+1}, t) = \hat{\phi}_\alpha(Z_n, t) \quad (7.1)$$

$$\hat{\phi}_\alpha^{(n)}(\eta_1, \eta_2, \dots, \eta_{n_s+1}, t) = \frac{1}{m_{Z_n}} \sum_{n=1}^{N_{Z_n}} \{m^{(n)}(i, j, k, t) \phi_\alpha^{(n)}(i, j, k, t) \mid Z_{id}^{(n)}(i, j, k, t) = Z_n\} \quad (7.2)$$

where  $m_{Z_n} = \sum_{n=1}^{N_{Z_n}} \{m^{(n)}(i, j, k, t) | Z_{id}^{(n)}(i, j, k, t) = Z_n\}$  is the total mass in the  $Z_n$ -th zone of the phase space and  $N_{Z_n}$  is the total number of cells mapped into the  $Z_n$ -th phase space zone. The mass-averaged  $\hat{\phi}_\alpha(Z_n, t)$  is the composition vector which is used during the chemistry integration operation step. The results upon integration are subsequently assigned to all cells in the zone  $Z^{(n)}$ . Errors due to mapping and mass averaging can be minimised by refining the phase space resolution. Sensitivity studies in the previous works show that a thermodynamic space of  $(T, \xi, \chi, Y_{fuel})$  is sufficient to uniquely map CFD cells of a partially premixed combustion case, where  $T$  is temperature,  $\xi$  is the Bilger mixture fraction,  $\chi$  is an analogy of the scalar dissipation rate and  $Y_{fuel}$  is the fuel mass fraction. Bilger's mixture fraction for the  $n$ -th field,  $\xi^{(n)}$ , is

$$\xi^{(n)} = \frac{0.5(J_H^{(n)} - J_{H,o})/W_H + 2(J_C^{(n)} - J_{C,o})/W_C - (J_O^{(n)} - J_{O,o})/W_O}{0.5(J_{H,f}^{(n)} - J_{H,o})/W_H + 2(J_{C,f}^{(n)} - J_{C,o})/W_C - (J_{O,f}^{(n)} - J_{O,o})/W_O} \quad (8)$$

where  $J_H$ ,  $J_C$  and  $J_O$  are element mass fractions,  $W_H$ ,  $W_C$  and  $W_O$  are the molecular weight of hydrogen, carbon and oxygen elements respectively. Subscripts “o” and “f” indicate the oxidizer and fuel streams respectively. The variable  $\chi^{(n)}$  is defined based on the gradient of the mixture fraction,  $\xi^{(n)}$  at each field as:

$$\chi^{(n)} = 2 \left( \bar{D} + \frac{\mu_t}{Sc_t} \right) \nabla \xi^{(n)} \cdot \nabla \xi^{(n)} \quad (9)$$

where  $\bar{D}$  is the molecular diffusion coefficient. Since it is an analogy to the scalar dissipation rate, it is exponentially decaying along the downstream direction in the mixing region of a free jet. Discretising the phase space in the  $\chi$  coordinate with uniform  $\Delta\chi$  is hence inefficient. Instead,  $\exp(-\chi)$  is used as the phase-space variable, implying that discretising phase space in the  $\chi$  coordinate with a non-uniform grid. For all other variables, a uniform grid is employed. The resolutions of the

thermodynamic space of  $(T, \xi, \chi, Y_{fuel})$  are fixed at 5 K, 0.01, 0.025 and 0.001 respectively in the current work.

### 3.2.3 Soot modelling

The ESF-CCM solver is incorporated with a two-equation, four-step soot model [18]. Productions of participating species (soot precursor, surface growth species and oxidants) are first calculated based on the gas-phase reactions and their resulting mean concentrations are imported into the governing equations of the soot model *i.e.* the transport equations for soot mass fraction,  $Y_{soot}$  and particle number density,  $N_{soot}$ .

$$\frac{\partial}{\partial t}(\rho Y_{soot}) + \nabla \cdot (\rho \vec{v} Y_{soot}) = \nabla \cdot \left( \frac{\mu_t}{Sc_t} \nabla Y_{soot} \right) + \frac{dM}{dt} \quad (10)$$

$$\frac{\partial}{\partial t}(\rho N_{soot}) + \nabla \cdot (\rho \vec{v} N_{soot}) = \nabla \cdot \left( \frac{\mu_t}{Sc_t} \nabla N_{soot} \right) + \frac{1}{N_A} \frac{dN}{dt} \quad (11)$$

The source term for soot mass fraction transport equation,  $\frac{dM}{dt}$  denotes the net soot production and is modelled by the expression,

$$\frac{dM}{dt} = MW_c \left( 100 \cdot \omega_{inc} + 2 \cdot \omega_{sg} - \omega_{OH} - \omega_{O_2} \right) \quad (12)$$

where  $MW_c$  is molecular weight of carbon. The first term on r.h.s. of Eq. (12) is the reaction rate of soot inception process while the second term represents the surface growth rates. The last two terms on the r.h.s. of Eq. (12) account for the soot oxidation rates due to OH and O<sub>2</sub> respectively. Here, C<sub>2</sub>H<sub>2</sub> is set as the soot precursor and surface growth species while OH and O<sub>2</sub> are chosen as soot oxidants. The source term of the particle number density transport equation,  $\frac{dN}{dt}$  is the instantaneous production rate of soot particles, which is subjected to inception from the gas phase and coagulation in the free molecular regime and it is computed using Eq. (13). The first term on the r.h.s. is the

multiplication of Avogadro constant,  $N_A$  and inception rate,  $\omega_{inc}$  as introduced earlier while the second term is a sink term due to coagulation.

$$\frac{dN}{dt} = N_A \cdot \omega_{inc} - \omega_{coag} \quad (13)$$

All the soot sub-models, which were optimised in the previous work [29] are used here. The formulation can be found in Table 3. Therein,  $T$  represents the gas temperature while  $\rho_{soot}$  denotes the density of soot. Apart from these, another important parameter in the modelling of soot formation is the associated soot specific surface area,  $S_{soot}$ . In the model, the inception rate is independent of this parameter but the surface growth rate and oxidation rate is a square root function of this parameter.

Table 3. The soot formation and oxidation sub-models [29].

Physical processes	Mathematical expressions
Inception	$\omega_{inc} = 10000 \cdot \exp\left(\frac{21000}{T}\right) \cdot [C_2H_2]$
Surface growth	$\omega_{sg} = 14 \left(\frac{P}{P_{ref}}\right)^{1.4} \cdot \exp\left(\frac{12100}{T}\right) \cdot S_{soot}^{0.5} \cdot [C_2H_2]$
Coagulation	$\omega_{coag} = 3.0 \left(\frac{24RT}{\rho_{soot} N_A}\right)^{0.5} \left(\frac{6M}{\pi \rho_{soot}}\right)^{1/6} N_{soot}^{11/6}$
OH oxidation	$\omega_{OH} = 1.146 \cdot T^{0.5} \cdot S_{soot} \cdot [OH]$
O <sub>2</sub> oxidation	$\omega_{O_2} = 10000 \cdot T^{0.5} \cdot \exp\left(\frac{19778}{T}\right) \cdot S_{soot} \cdot [O_2]$

### 3.3 Chemical kinetic mechanisms

For the modelling of *n*-dodecane Spray A, the skeletal mechanism developed by Yao et. al [61] is employed here. This mechanism was used with the L-tPDF by Christy [32] and Bolla [44, 45], allowing a comparison of the performance of the ESF-PDF method and its Lagrangian counterpart. The selection of a D2 surrogate fuel model depends on the objective of the numerical study. When the study aims to predict the diesel combustion and soot formation, the use of multi-component diesel surrogate models where aromatic and cyclo-paraffin chemistry are taken into consideration is essential [33,35,62-64]. However, the improved results with these multi-component diesel surrogate

models always come with a significant computational overhead since they commonly consist of a greater number of chemical species. Thus, a balance between computational efficiency and accuracy needs to be carefully considered when selecting a surrogate model for a given task. This work mainly aims to simulate the TCI effects on the flame structure, ignition delay time and lift-off length. The soot modelling is carried out to assess its performance in predicting the overall soot temporal/spatial distribution but not replicating the absolute value of the soot concentration. Hence, the single component surrogate fuel, *n*-heptane, which has a cetane number (CN) of around 55 that is comparable to the diesel fuel's CN, is considered here. The D2 fuel spray combustion under the Spray A condition, to date, is not widely studied. Hence, three skeletal *n*-heptane mechanisms, which were also commonly evaluated together with other TCI models [20,23,25], are examined in Section 4.1.1. Details about these mechanisms can be found in Table 4.

Table 4. Backgrounds of the chemical kinetic mechanisms evaluated in the current work.

Developer(s)	Number of species	Number of reactions	TCI model
Patel and Reitz [65]	29	52	L-tPDF
Liu et al. [66]	44	112	L-tPDF, CMC
Lu and Law [67]	68	258	L-tPDF, CMC

### 3.4 Numerical schemes and computational domain

The convection term is discretised with an upwind differencing scheme, while a central differencing scheme is applied for the diffusion term. The Semi-Implicit Bulirsch-Stoer scheme is used to solve the Ordinary Differential Equations. It is noticed that numerical instabilities occur for certain test condition when a pseudo 2-D mesh was employed. Instead, a 90 degree sector domain is used to represent the constant volume chamber which has a cubic shape with side lengths of 108 mm [68]. The injector is placed at the intersection of two cyclic boundaries. For the reference mesh, the minimum isotropic cell size is set to 0.5 mm within the spray combustion region. The mesh resolution is designed to be coarser outside the spray combustion region to reduce computational

runtime. The computational grid consists of approximately 89,000 cells. A mesh independence study performed for the current combustion simulation shows that further refinement to 0.25 mm x 0.25 mm x 0.25 mm does not give significant difference in the results; however, with the use of a 1.0 mm x 1.0 mm x 1.0 mm mesh, the ignition delay time is overestimated while the lift-off length is underestimated, as compared to those of the finer resolutions. The time step size is fixed at 0.2  $\mu$ s, which is found to reach stability without comprising the computational cost (not shown).

## 4. Sensitivity study

### 4.1 ECN Spray A condition

#### 4.1.1 Chemical kinetic mechanisms

The sensitivity study is first performed using the D2 case under the Spray A condition (case 4) to evaluate the performance of different chemical kinetic mechanisms. In these simulations, sixteen stochastic fields are employed and the  $C_\phi$  value is set to 2. This is similar to the configuration used by Gong et al. [38]. As shown in Fig. 2, the lift-off lengths of the established flames are consistently overestimated for all the chemical mechanisms when TCI is not taken into consideration. Although the 29 species mechanism predicts similar ignition delay time and lift-off length, the  $\text{CH}_2\text{O}$  distribution appears to be wider as compared to the other two mechanisms. Besides that, a substantial amount of  $\text{C}_7\text{H}_{15}\text{O}_2$  was observed about 100  $\mu$ s after the start of injection (ASI), indicating that the low-temperature reaction takes place much earlier. On the other hand, the 44 species and 68 species mechanisms predict that  $\text{C}_7\text{H}_{15}\text{O}_2$  increases significantly only after 400  $\mu$ s, which agrees better with the experimental observation [8] (as shown in Section 5.1.2 later). The 44 species mechanism is used in the subsequent simulations as it gives the best compromise between accuracy and computational efficiency.

#### 4.1.2 Mixing constant, $C_\phi$

The mixing constant,  $C_\phi$  is traditionally set to 2. In various flame modelling studies using the RANS-PDF approach,  $C_\phi$  is calibrated to different values at the vicinity of 2 [69,70]. Blouch et al. [71] and Cao et al. [72] also investigated a wider range of 1.5 to 3.8 and 0.75 to 6.0 respectively. In the modelling of diesel spray combustion, an even wider range of values has been reported. For instance, Pei et al. [19,20] in the modelling work of Sandia spray flames using the L-tPDF model, studied the effect of  $C_\phi$  ranging from 1 to 8. Also, Kung and Haworth [73] reported values ranging from 2 to 20 in the simulations of conventional diesel engine and premixed charge compression ignition combustion. These large variations in  $C_\phi$  likely result from a combination of the failure to compute the hydrodynamic time scale (or dissipation rate) correctly and the inherent limitations of single-timescale models. Here, the hydrodynamic timescale  $\tau$  is determined by a  $k-\varepsilon$  turbulence model ( $\tau = k/\varepsilon$ ), and the shortcomings of such models are well known [49,73]. Effects of  $C_\phi$  have been evaluated based on combustion related quantities in the aforementioned spray combustion simulations under engine-like conditions and engine combustion simulations [19,20, 73]. Based on lift-off lengths in [19,20] and pressure histories in [73], the PDF results in the limit  $C_\phi \rightarrow \infty$  were found to approximate to those of the WSR model.

In the current sensitivity study,  $C_\phi = 2$  is set as the reference case and is varied to evaluate its effects. Results in Fig. 3 show that the ignition delay time increases by approximately 0.1 ms when  $C_\phi$  was varied by a factor of thirty-two from 0.5 to 16. Under this condition, the ignition occurs at a region where the scalar dissipation rate is lower than that in the regions further upstream and away from the spray axis (where the flame is eventually stabilised). On the other hand, the lift-off lengths increase more significantly in the range of  $1 < C_\phi < 4$ . For  $C_\phi > 4$  the lift-off lengths become less sensitive to  $C_\phi$ . The sensitivity of lift-off length to  $C_\phi$  decreases with an increasing  $C_\phi$  as it

approaches the well-mixed limit and the lift-off lengths predicted used  $C_\phi > 4$  are close to that given by the WSR model (See. Fig. 2). This trend is in good agreement with that reported in the L-tPDF simulations, in which the effects of the mixing constant of the Euclidean minimum spanning trees micro-mixing model were investigated [19,20]. It should be mentioned that this sensitivity study aims to demonstrate that the ESF model reproduces the trend given by L-tPDF but not to calibrate  $C_\phi$  to match the experimental lift-off length. Considering that the formulation of the micro-mixing model is beyond the scope of this work, the traditional  $C_\phi$  value of 2 is used for all the subsequent simulations.

#### 4.1.3 Number of stochastic fields, $n_{sf}$

In a stochastic method, the number of samples has to be large enough to ensure that the results converge *i.e.* independent of the number of samples. Thus, the next parameter investigated in the sensitivity study is the number of stochastic fields ( $n_{sf}$ ). Jaishree and Haworth [51], who made comparisons between the Lagrangian and Eulerian-based transported PDF methods in the simulations of non-premixed pilot methane/air turbulent jet flames, revealed that a higher number of stochastic fields in the Eulerian method is essential for convergence. However, in the Valino's ESF PDF method, the Eulerian fields remain spatially smooth [50]. Therefore, it may be expected that the number of Eulerian fields required for converged statistics in the ESF method could be smaller than the number of particles per cell required for converged statistics in the L-tPDF method. In Refs. [19,22], the convergence study was evaluated based on ignition delay times and lift-off lengths. A similar evaluation is carried out here. In addition, comparisons of the pressure rise and temperature distribution calculated using different  $n_{sf}$  are also carried out here. Figures 4 and 5 display that the ignition delay times calculated based on 2, 4, 8, 16, 32, 64 and 128 stochastic fields are similar,

indicating these quantities are less sensitive to  $n_{sf}$ . However, as depicted in Fig. 5, fluctuations are observed for the pressure rise profiles modelled using only 2 and 4 stochastic fields. The fluctuations reduce with the increase of  $n_{sf}$ . Figure 4 also demonstrates that the lift-off lengths predicted using 8 or more stochastic fields are close to that of 128 fields, with the 64 stochastic field's result shows the best agreement with the results of 128 fields. Figure 6 depicts that, with the use of 2 and 4 stochastic fields, the corresponding stabilised flame structures are different from those of higher  $n_{sf}$ . The temperature profiles along the spray axis and across the diffusion flame as illustrated in Fig. 6 are next compared to quantify the relative difference. In addition, carbon monoxide (CO) and CH<sub>2</sub>O mass fractions along the spray axis as well as carbon dioxide (CO<sub>2</sub>) and OH mass fractions across the diffusion flame are also used to evaluate the convergence of the results with respect to variations of  $n_{sf}$ . OH and CH<sub>2</sub>O are selected because they reflect the high- and low-temperature chemistries respectively, while CO<sub>2</sub> and CO are important species in the diffusion flame and the rich premixed flame respectively. The extended convergence studies are carried out since these quantities will be used to analyse the diesel spray flame structure (to be shown in Section 6).

As demonstrated in Fig. 7, the flame structure of 2 stochastic fields is significantly different from those generated using higher  $n_{sf}$ . Although those of 4 and 8 stochastic fields show a general stabilised flame, the fuel-rich region combustion product CO and CH<sub>2</sub>O appear to be narrower. Besides that, the diffusion flame of the 4 fields also appears to be broader as shown by the associated temperature and CO<sub>2</sub> profiles. The relative differences of peak temperature as well as peak mass fractions of the selected species are evaluated based on the results generated using 128 stochastic fields and are quantified using Eq. (14).

$$relative\ difference = \frac{|\alpha_{n_{sf},i} - \alpha_{n_{sf},base}|}{\alpha_{n_{sf},base}} \times 100\% \quad (14)$$

where  $\alpha$  represents different combustion properties and  $i$  denotes different  $n_{sf}$ . It is found that the maximum relative difference reaches 40% for 8 stochastic fields and remains within 10% for 16, 32 and 64 stochastic fields. It is noteworthy that the use of 16 and 32 stochastic fields predicts longer lift-off lengths (which may influence the prediction of the air entrainment). Yet, Fig. 7(a) depicts that the associated prediction of the fuel-rich region combustion product, CO, is similar to those of higher stochastic fields. Besides this, the soot precursor and surface growth species,  $C_2H_2$ , predicted by 16 or greater number of stochastic fields is found to be similar as well (See Fig. A1 in Appendix A).

## 4.2 Low and high temperature conditions

The sensitivity study is extended to the 800 K and 1100 K conditions at the ambient density of 14.8 kg/m<sup>3</sup>, which are used to represent the low- and high-ambient temperature conditions respectively. The sensitivity study is carried out for both 15% and 21% O<sub>2</sub> levels using 16, 32 and 64 stochastic fields. These configurations are selected as they reach a balance between computational efficiency and convergence. Here, 64 stochastic field results serve as the baseline for comparison purpose. Under these four conditions, the ignition delay time and lift-off length are similar (not shown). Figure 8 illustrates that the temperature and species profiles for the 15% O<sub>2</sub> condition predicted using both the 16 and 32 stochastic fields are found to converge reasonably well, with a maximum relative difference of 19%. Figure 9 shows the comparisons of temperature and species profiles for the 21% O<sub>2</sub> condition. As shown, those of 16 stochastic fields have a maximum value of relative differences of 41% and 18% for the ambient temperatures of 800K and 1100K cases respectively. On the other hand, the associated relative differences of 32 stochastic fields remain within 27% and 4% at  $T_{am} = 800$  K and 1100 K respectively.

In general, when the ignition delay time and lift-off length are used for basis of comparison, the dependence of  $n_{sf}$  is small for  $n_{sf}$  of 8 and above. Yet, when temperature and species profiles along the spray axis and across the established flames are compared, it is found that the results

1 predicted using 32 stochastic fields achieves the best compromise between convergence and  
2 computational efficiency. This is close to the nominal number of PDF particles per finite-volume cell  
3 of 30 used by Bhattacharjee and Haworth [22], which was selected based on the lift-off length results  
4 from convergence studies. With the use of ten 64-bit Intel Ivy Bridge Xeon E5-2650 v2 8-core CPUs  
5 running at 2.60 GHz [74], the computational runtime consumed by the 32 stochastic fields for case 4  
6 is approximately 140 hours to simulate the combustion process of 1.5 ms. The results predicted using  
7 the 32 stochastic fields are validated using the experimental data and discussed in the subsequent  
8 section.  
9  
10  
11  
12  
13  
14  
15  
16  
17  
18  
19  
20  
21

## 22 **5. Model validation**

### 23 **5.1 ECN Spray A condition**

#### 24 *5.1.1 Comparisons of ignition delay and lift-off length*

25 Ignition delays and lift-off lengths during quasi-steady state predicted by the ESF model are  
26 compared with the experimental measurements for both *n*-dodecane and D2 fuels. The WSR results  
27 are also included to illustrate the effects of TCI. Figure 10 demonstrates that the WSR model predicts  
28 consistently longer ignition delays and lift-off lengths, in which the maximum relative difference is  
29 67%. On the other hand, using the ESF as the TCI closure approach improves the predictions, with  
30 the maximum relative difference remains within 14% in these cases. Comparisons with the literature  
31 shows that the ignition delay in case 3 predicted in the current work is 0.35 ms, which is similar to  
32 that predicted by Christy et al. [32] and Bolla et al. [44,45]; while the lift-off length simulated here is  
33 shorter than theirs. It is also noted that the mixture in both the WSR cases ignite later; the associated  
34 flame lift-off positions are stabilised near the ignition site locations and they do not propagate  
35 towards the injection tip as observed in the experiment.  
36  
37  
38  
39  
40  
41  
42  
43  
44  
45  
46  
47  
48  
49  
50  
51  
52  
53  
54  
55

56 The simulated OH distributions of the D2 cases are compared in Fig. 11. The OH  
57 distributions predicted using the ESF model are consistently broader and resemble the experimental  
58  
59  
60  
61  
62  
63  
64  
65

observation. The WSR model predicts physically implausible turbulent flame structures. Similarly, it is noted that the O radicals distribution predicted by the ESF model is also wider than that by the WSR model. It is expected that such differences would affect the prediction of pollutant formation. For instance, NO<sub>x</sub> formation through the Zeldovich mechanism depends strongly on the concentrations of O and OH radicals [79]. It is also expected that the SO<sub>x</sub> predictions will be sensitive to the TCI models, since sulphur dioxide (SO<sub>2</sub>) formed (from the fuel sulphur) is subsequently oxidised to sulphur trioxide (SO<sub>3</sub>) through the reaction with O radicals [16] in air-excessive heavy fuel oil combustion in marine engines.

### 5.1.2 Transient spray flame and soot development

The transient spray flame and soot development of case 4 recorded from the experiment is displayed in Fig. 12(a). The non-reacting jet boundary (marked as red solid line), which was obtained by separate shadowgraph imaging for a particular injection, is also shown on the reacting jet shadowgraph images. The blue solid line overlaid on the shadowgraph image is the liquid-phase fuel, captured by a separate high-speed imaging of the Mie-scattering [8]. The simulated soot volume fraction contour is provided in Fig. 12(b). The iso-contour in red is used to represent the fuel vapour from the separate non-reacting spray simulation (case 2, cf. Table 2), while the green and yellow iso-contours denote the C<sub>7</sub>H<sub>15</sub>O<sub>2</sub> mass fraction of  $5 \times 10^{-4}$  and temperature of 1300 K respectively. The experimental premixed burn event is indicated using the Takeno's flame index (FI) [75]. Different interpretations have been suggested based on the Takeno's FI [1,10]. Here, a FI similar to that proposed in Refs. [76,77] is used; thus, the premixed flame can be identified for both fuel-lean and fuel-rich conditions. The only difference here is that the local equivalence ratio is used instead of mixture fraction, as shown in Eq. (15),

$$FI = \frac{\nabla Y_F \cdot \nabla Y_O}{|\nabla Y_F \cdot \nabla Y_O|} \cdot \frac{\phi - 1}{|\phi - 1|} \quad (15)$$

where the mass fraction of fuel,  $Y_F$  includes those of evaporating species,  $n$ -heptane as well as the main fuel-rich combustion products, *i.e.* CO and H<sub>2</sub>. Although Pei et al. [10] suggested that other fuel-rich combustion products such as C<sub>2</sub>H<sub>2</sub>, CH<sub>4</sub>, CH<sub>3</sub> and CH<sub>2</sub> have to be taken into account, a sensitivity study shows that these species do not influence the FI profile significantly and the discussion presented later does not change with the additional consideration of the aforementioned species. In Eq. (15) the mass fraction of the oxidiser,  $Y_O$ , is represented by that of O<sub>2</sub>. In the modified FI, -1 and 1 represent the lean premixed flame and the rich premixed flame respectively. In the current work, EGR is taken into consideration. The equivalence ratio,  $\phi$  is computed as

$$\phi = \frac{Y_{C,P} - Y_{C,E} + Y_{H,P} - Y_{H,E} + \theta (Y_{H,P} - Y_{H,E})}{[Y_{O,P} - Y_{O,CO_2,E} - Y_{O,H_2O,E} - \theta (Y_{H,P} - Y_{H,E})](F/O)_{st}} \quad (16)$$

where  $Y$  is the elemental mass fraction. Subscripts  $C$ ,  $H$ ,  $O$  represent carbon, hydrogen and oxygen atoms respectively, while subscripts  $P$  and  $E$  denote the composition of combustion products and EGR respectively. The stoichiometric fuel to oxygen ratio is represented by  $(F/O)_{st}$  while  $\theta$  is the ratio of oxygen to hydrogen in the fuel composition. Derivation of Eq. (16) is similar to that presented by Zhang et al. [78] and is provided in Appendix B. In Fig. 12(b), the purple iso-contour, which represents the modified FI of 0.9, is used to represent the rich premixed flame.

As depicted in Fig. 12, the reacting jet undergoes the low-temperature reaction starting at about 500 through 650  $\mu$ s after the start of injection (ASI). High-temperature combustion and the premixed burn then begin to appear at about 950  $\mu$ s ASI as indicated by the expansion of the jet due to intense heat release. The soot cloud is apparent in the experiment at approximately 1307  $\mu$ s at the downstream flame front, approximately 45 mm away from the injection tip. The soot cloud grows in size around the site of soot onset as the combustion progresses. At about 1800  $\mu$ s, the soot cloud expands to approximately 65 mm. The transient flame and soot developments are well captured by the model.

Figure 13 depicts the soot volume fraction (SVF) distribution at quasi-steady state in the D2 cases at 900 K and 1000 K. Comparisons with the experimental results show that the spatial distribution is reasonably well predicted by the ESF model. The experimental maximum SVF rises by approximately five-fold as the ambient temperature is increased from 900 K to 1000 K [7]. This ratio is henceforth represented by  $\zeta_{SVF}$  for brevity. The  $\zeta_{SVF}$  calculated by the current model is less than two. As aforementioned, the difference in the predicted and measured  $\zeta_{SVF}$  is attributed to the absence of aromatic kinetics in the soot mechanism employed in this study [43].

## 5.2 Ambient temperature variation

This section aims to further validate the models across a wider range of ambient temperatures at different ambient density and O<sub>2</sub> levels using the experimental ignition delays and lift-off lengths [2,3]. A relative error metric,  $\eta$  as shown by Eq. (17) is used to characterise the overall performance of the ESF model at each temperature sweep [20].

$$\eta = \frac{\sqrt{\sum (\alpha_{sim} - \alpha_{exp})^2}}{\sum \alpha_{exp}} \cdot 100\% \quad (17)$$

Here,  $\alpha_{sim}$  and  $\alpha_{exp}$  represent the simulated and experimental ignition delay time (or lift-off length) respectively. Ignition delay time and lift-off length computed using the WSR model are also discussed to single out and quantify the effects of TCI.

### 5.2.1 Diesel combustion at low pressure, with exhaust gas recirculation

The first set of temperature sweep is carried out for the operating conditions of 15% O<sub>2</sub> (*i.e.* with EGR) and ambient density of 14.8 kg/m<sup>3</sup>. The ambient pressures in these cases vary from 33 bar to 50 bar and the test cases are categorised as the low-pressure cases. The results in Fig. 14(a) depict that the ignition delay time prediction is dependent on the TCI. Although both ESF and WSR models predict higher ignition delay time as compared to the measurements, the relative error for ESF is

lower at 10% while that of WSR increases to 18%. Figure 14 (b) shows that the ESF model predicts more accurate lift-off lengths for ambient temperatures of 900 K and above. In the 800 K case, the lift-off position is found to gradually propagate upstream (towards the injector direction), yielding an underestimated lift-off length. Yet, the relative error across the tested ambient temperatures is lower at 13% for the ESF model and the value increases to 17% for WSR model where TCI is not considered.

### 5.2.2 Diesel combustion at low pressures, without exhaust gas recirculation

Next, the ambient  $O_2$  level is increased to 21%, imitating the engine condition without EGR. Figure 15 displays that the TCI affects the predictions of both ignition delay time and lift-off length. For this temperature sweep, the relative differences of the ignition delay time and lift-off length at each tested condition remain within 30%, apart from those in the 800 K case where the relative difference are approximately 50%. The associated lift-off position is found to gradually propagate upstream as the ambient temperature increases, which is similar to that in the 15%  $O_2$  and 800 K case as aforementioned. In general, the relative error of ignition delay time across the ambient temperatures predicted by the ESF and the WSR models are 18% and 24% respectively. As for the lift-off length, the relative error drops from 18% to 15% when the TCI effect is taken into account.

### 5.2.3 Diesel combustion at high pressures, without exhaust gas recirculation

The ambient density is increased from  $14.8 \text{ kg/m}^3$  to  $30.0 \text{ kg/m}^3$ , corresponding to ambient pressures varying from 68 to 93 bar. These are characterised as the high-pressure cases. Figure 16(a) shows that the ignition delay time calculated using ESF and WSR methods are almost identical. The relative errors are acceptable for ambient temperature of 850 K and above. Although the overall relative error is approximately 30%, the large relative error is mainly attributed by the difference obtained in the 800 K case. Figure 16(b) demonstrates that the lift-off lengths in the  $30.0 \text{ kg/m}^3$  test cases predicted

using the ESF model agree well with the experimental data, while the WSR model predicts longer lift-off lengths at all initial temperature conditions. The relative error for lift-off length predicted by the ESF and WSR models is 10% and 22% respectively.

In general, the trends of the ignition delay and lift-off lengths with respect to the change of operating conditions are reasonably well reproduced. Only at the lower temperatures, the use of the 44-species *n*-heptane chemical mechanism overpredicts the ignition delay and underpredicts the lift-off lengths. This observation is in line with the simulation results reported by Bolla et al. [25] when a different TCI closure approach, the CMC model was employed with the same mechanism for the same thermochemical conditions.

## 6. Flame structures

### 6.1 Temperature-equivalence ratio map

Figure 17 shows scatter plots of the CFD cells in the  $T$ - $\phi$  space, which depicts the evolution of the temperature ( $T$ ) and equivalence ratio ( $\phi$ ) during ignition process, ranging from the low-temperature ignition to the quasi-steady state burning stages. In the beginning, all the flow field remains at low  $T$ -low  $\phi$  and low  $T$ -high  $\phi$ . The former represents the ambient gas region while the latter characterises the region near the injector. Thereafter, a more apparent rise of temperature is observed at the fuel-lean mixture. The peak temperature reaches above 1300 K at 0.93 ms, indicating the onset of main ignition at fuel-rich mixture. The temperature of the fuel-rich mixture continues to increase and reaches above 2000 K at 1.05 ms. Soon after the onset of ignition the maximum temperature is found near the stoichiometric mixture. Here, the classical diesel spray flame proposed by Dec [80] is formed. The intermediate- $T$  and high- $\phi$  region in the figure denotes the fuel-rich premixed core while the outer diffusion flame has a  $\phi$  value of approximately one that is shown to have a higher temperature. The evolution of the  $T$ - $\phi$  map is the same as those reported in Refs. [10,22], although the operating conditions and fuel types are different. The evolution of the  $T$ - $\phi$  map is similar when

the WSR model is used, although the predicted ID is longer (not shown for brevity). However, a comparison between the WSR and ESF results at quasi-steady state shows that the region with high maximum temperature predicted by the ESF model is broader, extending to  $\phi$  of approximately 1.2. This agrees well with the observation that the OH distribution from the ESF model is broader. Also, within the fuel-rich, intermediate temperature region, the associated equivalence ratio is higher. This corresponds well with the shorter lift-off length and hence less air entrainment predicted by the ESF model.

## 6.2 Triple flames

As aforementioned, the structure of spray flames under engine-like condition may vary under different conditions. Jangi et al. [1] investigated a diesel spray flame at 21% O<sub>2</sub>, 1000 K and 14.8 kg/m<sup>3</sup>. They showed that when the flame stabilisation is reached, a triple flame is formed. In the simulation of a *n*-dodecane spray at 15% O<sub>2</sub>, 900 K and 22.8 kg/m<sup>3</sup> presented by Pei et al. [10], it was reported that the stabilised flame consists of a partially fuel-rich premixed flame and a diffusion flame. The combustion mode is investigated in this section.

Similar to the approach in Refs. [1,10], the modified FI is used to indicate the combustion mode. The lean premixed flame and the rich premixed flame are indicated respectively by black and light grey in Fig. 18. The dark grey denotes the non-premixed mode, where the stoichiometric mixture (represented by the green iso-contour) always falls into. Apart from FI, the spatial distribution of an intermediate combustion product, CH<sub>2</sub>O can also be used to indicate the development of the triple flame. Joedicke et al. [81] used the Laser induced pre-dissociation fluorescence of CH<sub>2</sub>O to monitor the lean reaction zone. The analysis of the total heat release rate shows that the main reactions contributing to the heat are the same in the triple flame and the premixed flame [82]. One of the most significant reactions in the main reaction zone is  $\text{CH}_3 + \text{O} \rightarrow \text{CH}_2\text{O} + \text{H}$ . The blue iso-contour plotted represents the CH<sub>2</sub>O mass fraction of 10% of the maximum

value at its respective time step. The yellow iso-contour represents chemical heat release rate of 1% of the maximum value at its respective time step. Besides, the red iso-contour of the temperature of 200 K above the ambient temperature is used to represent the reaction zones as suggested by Jangi et al. [1]. The transient development of these properties is depicted in Fig. 18.

In the initial stage, the distribution of  $\text{CH}_2\text{O}$  is wide, covering both the fuel-lean and the fuel-rich regions. The premixed fuel-rich mixture reaches the temperature above 1100 K at about 950  $\mu\text{s}$  ASI. This mixture undergoes high-temperature ignition at about 1000  $\mu\text{s}$  ASI, as shown by the reappearance and expansion of the jet by more intense heat release. Soon afterwards, at 1100  $\mu\text{s}$  ASI, the  $\text{CH}_2\text{O}$  near the stoichiometric line is consumed. An apparent triple flame structure is then formed at 1200  $\mu\text{s}$  ASI and remains until 1250  $\mu\text{s}$  ASI. Thereafter, the distribution of  $\text{CH}_2\text{O}$  is found to shrink, indicating that the lean premixed flame becomes weaker. Although a lean premixed flame is indicated by the FI, it could be an artefact since it falls out of the zone with high heat release rate. This is shown in the flame at 1450  $\mu\text{s}$  ASI. Such double-flame structure agrees with that reported by Pei et al. [10] who simulated the *n*-dodecane spray flame under the same operating condition as aforementioned. It is worth mentioning that, the behaviour of the triple flame remains the same when a larger number of stochastic fields are used.

The transient developments of flame structures in the low-pressure cases with different ambient temperature and  $\text{O}_2$  levels are next investigated. Figure 19 depicts the transient developments of flame structures in case 7 (800 K; 15%  $\text{O}_2$ ), case 11 (1100 K; 15%  $\text{O}_2$ ), case 12 (800 K; 21%  $\text{O}_2$ ), and case 16 (1100 K; 21%  $\text{O}_2$ ). In terms of FI, the change of the combustion mode observed in these cases resembles that under the Spray A condition. At high temperatures of 1100 K, it is noticed that the lean premixed flame or  $\text{CH}_2\text{O}$  shrinks faster. The lean premixed flame and  $\text{CH}_2\text{O}$  disappear within approximately 400  $\mu\text{s}$  and 300  $\mu\text{s}$  after their respective ignition time in the 15% and 21%  $\text{O}_2$  cases respectively. At the low initial temperature of 800 K, the triple flame remains for a longer time duration. For instance in the 800 K and 15%  $\text{O}_2$  case, the triple-flame structure is

still observed at approximately 1 ms after the ignition time. This can be attributed to the CH<sub>2</sub>O chemistry. At higher temperatures, the reactions of CH<sub>2</sub>O + M → HCO + H + M (where M is the species involved in third-body collision) and then H + O<sub>2</sub> → OH + O are more active [83]. The CH<sub>2</sub>O is consumed and OH is formed within the diffusion flame. These observations are similar in cases 17 and 22, where the ambient density increases to 30.0 kg/m<sup>3</sup>.

### 6.3 Transport budgets

The mechanism on the flame stabilisation is now investigated following an analysis proposed by Gordon et al. [84], based on comparisons of transport budget terms in the Favre-averaged species governing equations. The comparison of transport budgets [84] is carried out for the results obtained using 32 stochastic fields. The diffusion term is mainly governed by the turbulent diffusivity while the reaction rate is computed as Eq. (3) as aforementioned.

The results show that near the lift-off position, the reaction rate of OH is consistently much higher than the diffusion term, indicating that the flame is stabilised by the auto-ignition process (not shown). This agrees with the findings from the literature [10,38]. Similar to the transport budgets of OH, the reaction rates of CO<sub>2</sub> are consistently much higher than the diffusion rates near the lift-off position (see Fig. 20). The results show that the ambient O<sub>2</sub> level has a greater effect on the reaction rate than the ambient temperature does near the lift-off positions, where the peak reaction rates in both 21% O<sub>2</sub> cases are approximately two-fold higher than those in the 15% O<sub>2</sub> cases. On the other hand, the rates of diffusion and reaction are in the same order of magnitude downstream, indicating the existence of the diffusion flame. The rates of diffusion and reaction in the 1100 K cases are higher than those in the 800 K cases across the diffusion flames; while for the different ambient O<sub>2</sub> levels, the peak values are relatively close.

## 7. Concluding remarks

The Eulerian based probability density function (PDF) method has been validated for a wide range spray combustion conditions relevant to modern diesel engines. This method provides an alternative to Lagrangian particle PDF methods. The benefits of transported PDF methods are retained yet the complications of Lagrangian particle PDF methods can be avoided [22,50,51]. Here, the Eulerian Stochastic Field (ESF) model has been coupled with the Chemistry Coordinate Mapping (CCM) method to simulate auto-ignition and combustion of turbulent spray flames under a wide range of engine-relevant thermochemical conditions at an expedited calculation. A skeletal mechanism consisting of 44 species is used as the diesel surrogate fuel model. A comprehensive convergence study was carried out for the number of stochastic fields,  $n_{sf}$ . The performance of the model is first evaluated based on ignition delay time, lift-off length and flame structure under the Spray A condition. It is noticed that although the use of 8 stochastic fields predicts reasonable ignition delay time and lift-off lengths, the associated flame structures are different from those predicted using 16, 32, 64 and 128 stochastic fields. The 16, 32 and 64 stochastic fields are then used in the extended convergence study. The ignition delay time and lift-off length predicted using 16 and 32 stochastic fields are found reasonably close to those of higher number of stochastic fields. The temperature and species concentration fields predicted using 32 stochastic fields are found to converge, where the relative difference remains within 27%. For other conditions where the ambient oxygen (O<sub>2</sub>) level is higher at 21% and the ambient temperature is higher at 1100 K, the relative error calculated using the 32 stochastic fields has a maximum value of 4%. The convergence achieved by 32 stochastic fields agrees with the nominal number of PDF particles per finite-volume cell of 30 used by Bhattacharjee and Haworth [22], which was selected based on lift-off length results from convergence studies.

Numerical results from the ESF model with 32 stochastic fields are further compared with the Engine Combustion Network (ECN) experimental data of *n*-dodecane and diesel fuels collected under the Spray A condition. The ESF results are also compared with those from a locally Well-

1 Stirred Reactor (WSR) model, where turbulent fluctuations in composition and temperature about  
2 their local mean values are neglected. This aims to isolate and quantify the effects of turbulence-  
3 chemistry interaction (TCI). When the ESF is used as the TCI closure approach, predictions of both  
4  
5 chemistry interaction (TCI). When the ESF is used as the TCI closure approach, predictions of both  
6  
7 ignition delay times and lift-off lengths are improved. Besides that, the ESF model also predicts a  
8  
9 broader hydroxyl radicals (OH) distribution that resembles the experimental observation while the  
10  
11 WSR model produces physically implausible turbulent flame structures. The simulated transient  
12  
13 flame and soot development also agree with the measurements.  
14  
15

16  
17 The model validation is then extended using measured ignition delay times and lift-off  
18  
19 lengths recorded for the diesel fuel across a wider range of ambient temperatures at different ambient  
20  
21 oxygen concentration and pressure levels. TCI is found to have greater effects on ignition delay time  
22  
23 prediction in cases with low pressure. The computed ignition delay times from the WSR and ESF  
24  
25 models are similar in the high-pressure cases. Besides that, the lift-off lengths predicted by the ESF  
26  
27 model are in general more accurate than those from the WSR model, with the relative error of lift-off  
28  
29 length from the ESF model remains below 15% for all the tested conditions. A lower relative error  
30  
31 can be expected when the predictions of lift-off lengths in the low-pressure, low-temperature (below  
32  
33 900K) cases are improved. On the contrary, the relative errors of lift-off lengths predicted by the  
34  
35 WSR model vary from 17% to 22%. The thermochemical conditions examined here cover those of  
36  
37 light duty, heavy duty and marine diesel engines.  
38  
39  
40  
41  
42

43  
44 Analyses based on flame index and formaldehyde distribution are performed for the Spray A  
45  
46 condition to investigate the spray flame structure. It is noticed that a triple flame forms in the earlier  
47  
48 stage of the combustion phase but it weakens. A double-flame structure, consisting of a diffusion  
49  
50 flame and a rich premixed flame is observed as combustion progresses. The pattern is similar for  
51  
52 cases with higher ambient temperature, despite the different ambient pressures and/or ambient O<sub>2</sub>  
53  
54 levels. The life span of the lean premixed flame is, however, shorter for the higher ambient  
55  
56 temperature cases. On the other hand, at the ambient temperature of 800 K, the triple flame remains  
57  
58  
59  
60

1 for a longer time period. For instance in the 800 K and 15% O<sub>2</sub> case, the triple-flame structure is still  
2 observed at approximately 1 ms after the ignition time. The triple flame behaviours remain the same  
3 at higher ambient pressures.  
4  
5

6  
7 The transport budget shows that the reaction rates of OH and CO<sub>2</sub> are consistently much  
8 higher than their diffusion rates near the lift-off position in all test cases, indicating that the flames  
9 are stabilised by the auto-ignition process. It is also noticed that the ambient O<sub>2</sub> level has a greater  
10 effect on the reaction rate than the ambient temperature does near the lift-off positions. On the other  
11 hand, the rates of diffusion and reaction are in the same order of magnitude downstream, indicating  
12 the existence of the diffusion flame.  
13  
14  
15  
16  
17  
18  
19  
20  
21  
22  
23

## 24 **Acknowledgements**

25  
26 The authors gratefully acknowledge the financial support from the Innovation Fund Denmark and  
27 MAN Diesel & Turbo through the SULCOR project. The computation was performed using Abisko  
28 cluster at High performance Computing Center North (HPC2N, Sweden) and Niflheim cluster at  
29 Technical University of Denmark (DTU). The authors would also like to thank Dr. Tianfeng Lu from  
30 the University of Connecticut for sharing the skeletal *n*-dodecane mechanism.  
31  
32  
33  
34  
35  
36  
37  
38  
39  
40

## 41 **References**

- 42  
43 1. M. Jangi, T. Lucchini, C. Gong, X.-S. Bai, Effects of fuel cetane number on the structure of  
44 diesel spray combustion: An accelerated Eulerian stochastic fields method, *Combust. Theory*  
45 *Model.* 19 (2015) 549-567.  
46  
47  
48  
49  
50
- 51 2. Engine Combustion Network. Available at <http://www.sandia.gov/ecn/>  
52  
53
- 54 3. D. Siebers, B. Higgins, L. Pickett, Flame Lift-Off on Direct-Injection Diesel Fuel Jets: Oxygen  
55 Concentration Effects, SAE Technical Paper 2002-01-0890, 2002.  
56  
57  
58  
59

4. L. Pickett, C. Genzale, G. Bruneaux, L. Malbec, L. Hermant, C. Christiansen, J. Schramm, Comparison of diesel spray combustion in different high-temperature, high-pressure facilities, SAE Int. J. Engines 3 (2010) 156-181.
5. L.M. Pickett, D.L. Siebers, Soot in diesel fuel jets: effects of ambient temperature, ambient density, and injection pressure, Combust Flame 138 (2004) 114-135.
6. J.G. Nerva, C.L. Genzale, S. Kook, J.M. Garcia-Oliver, L.M. Pickett, Fundamental spray and combustion measurements of soy methyl-ester biodiesel, Int. J. Engine Research 14 (2013) 373-390.
7. S. Kook, L.M. Pickett, Soot volume fraction and morphology of conventional and surrogate jet fuel sprays at 1000-K and 6.7-MPa ambient conditions, Proc. Combust. Inst. 33 (2011) 2911-2918.
8. S. Kook, L.M. Pickett, Effect of fuel volatility and ignition quality on combustion and soot formation at fixed premixing conditions, SAE Int. J. Engines 2 (2010) 11-23.
9. M.P.B. Musculus, P.C. Miles, L.M. Pickett, Conceptual models for partially premixed low-temperature diesel combustion, Prog. Energy Combust. Sci. 39 (2013) 246-283.
10. Y. Pei, E.R. Hawkes, M. Bolla, S. Kook, G.M. Goldin, Y. Yang, S.B. Pope, S. Som, An analysis of the structure of an *n*-dodecane spray flame using TPDF modelling, Combust. Flame 168 (2016) 420-435.
11. S. Hong, M.S. Wooldridge, H.G. Im, D.N. Assanis, H. Pitsch, Development and application of a comprehensive soot model for 3D CFD reacting flow studies in a diesel engine, Combust. Flame 143 (2005) 11-26.
12. K.M. Pang, N. Karvounis, J. Walther, J. Schramm, Numerical investigation of soot formation and oxidation processes under large two-stroke marine diesel engine-like conditions using integrated CFD-chemical kinetics, Appl. Energy 169 (2016) 874-887.

13. G. D'Errico, T. Lucchini, G. Hardy, F. Tap, G. Ramaekers, Combustion modeling in heavy duty diesel engines using detailed chemistry and turbulence-chemistry interaction, SAE Technical Paper 2015-01-0375, 2015.
14. H.J. Curran, P. Gaffuri, W.J. Pitz, C.K. Westbrook, A comprehensive modeling study of *n*-heptane oxidation, Combust. Flame 114 (1998) 149-177.
15. H. Guo, F. Liu, G.J. Smallwood, A numerical study on NO<sub>x</sub> formation in laminar counterflow CH<sub>4</sub>/air triple flames, Combust. Flame 143 (2005) 282-298.
16. L. Hindiyarti, P. Glarborg, P. Marshall, Reactions of SO<sub>3</sub> with the O/H radical pool under combustion conditions, J. Phys. Chem. A 111 (2007) 3984-3991.
17. D.R. Tree, K.I. Svensson, Soot processes in compression ignition engines, Prog. Energy Combust. Sci. 33 (2007) 272-309.
18. K.M. Leung, R.P. Lindstedt, W.P. Jones, A simplified reaction mechanism for soot formation in nonpremixed flames Combust. Flame 87 (1991) 289-305.
19. Y. Pei, E.R. Hawkes, S. Kook, A comprehensive study of effects of mixing and chemical kinetic models on predictions of *n*-heptane jet ignitions with the PDF method, Flow, Turbul. Combust. 91 (2013) 249-280.
20. Y. Pei, E.R. Hawkes, S. Kook, Transported probability density function modelling of the vapour phase of an *n*-heptane jet at diesel engine conditions, Proc. Combust. Inst. 34 (2013) 3039-3047.
21. Y. Pei, E.R. Hawkes, S. Kook, G.M. Goldin, T. Lu, Modelling *n*-dodecane spray and combustion with the transported probability density function method, Combust. Flame 162 (2015) 2006-2019.
22. S. Bhattacharjee, D.C. Haworth, Simulations of transient *n*-heptane and *n*-dodecane spray flames under engine-relevant conditions using a transported PDF method, Combust. Flame 160 (2013) 2083-2102.

23. M. Bolla, Y.M. Wright, K. Boulouchos, G. Borghesi, and E. Mastorakos, Soot formation modeling of *n*-heptane sprays under diesel engine conditions using the conditional moment closure approach, *Combust. Sci. Technol.* 185 (2013) 766-793.
24. M. Bolla, D. Farrace, Y.M. Wright, K. Boulouchos, E. Mastorakos, Influence of turbulence-chemistry interaction for *n*-heptane spray combustion under diesel engine conditions with emphasis on soot formation and oxidation, *Combust. Theor. Model.* 18 (2014) 330-360.
25. M. Bolla, T. Gudmundsson, Y.M. Wright, K. Boulouchos, Simulations of diesel sprays using the Conditional Moment Closure model, *SAE Int. J. Engines* 6 (2013) 1249-1261.
26. Y.M. Wright, G. De Paola, K. Boulouchos, E. Mastorako, Simulations of spray autoignition and flame establishment with two-dimensional CMC, *Combust. Flame* 142 (2005) 402-419.
27. A. Irannejad, A. Banaeizadeh, F. Jaber, Large eddy simulation of turbulent spray combustion, *Combust. Flame* 162 (2015) 431-450.
28. T. Lucchini, G. D'Errico, F. Contino, M. Jangi, Towards the use of Eulerian field PDF methods for combustion modeling in IC Engines, *SAE Int. J. Eng.* 7 (2014) 286-296.
29. K.M. Pang, M. Jangi, X.-S. Bai, J. Schramm, Evaluation and optimisation of phenomenological multi-step soot model for spray combustion under diesel engine-like operating conditions, *Combust. Theor. Model.* 19 (2015) 279-308.
30. H. Wang, Y. Ra, M. Jia, R.D. Reitz, Development of a reduced *n*-dodecane-PAH mechanism and its application for *n*-dodecane soot predictions, *Fuel* 136 (2014) 25-36.
31. C. Gong, M. Jangi, X.-S. Bai, Large eddy simulation of *n*-dodecane spray combustion in a high pressure combustion vessel, *Appl. Energy* 136 (2014) 373-381.
32. M. Chishty, M. Bolla, E. Hawkes, Y. Pei, S. Kook, Assessing the importance of radiative heat transfer for ECN Spray A using the transported PDF method, *SAE Int. J. Fuels Lubr.* 9 (2016) 100-107.

33. A. Frassoldati, G. D'Errico, T. Lucchini, A. Stagni, A. Cuoci, T. Faravelli, A. Onorati, E. Ranzi, Reduced kinetic mechanisms of diesel fuel surrogate for engine CFD simulations, *Combust. Flame* 162 (2015) 3991-4007.
34. X. Cheng, H.K. Ng, S. Gan, J.H. Ho, K.M. Pang, Development and validation of a generic reduced chemical kinetic mechanism for CFD spray combustion modelling of biodiesel fuels, *Combust. Flame* 162 (2015) 2354-2370.
35. H.M. Poon, K.M. Pang, H.K. Ng, S. Gan, J. Schramm, Development of multi-component diesel surrogate fuel models – Part II: Validation of the integrated mechanisms in 0-D kinetic and 2-D CFD spray combustion simulations, *Fuel* 181 (2016) 120-130.
36. G. Vishawanthan, R.D. Reitz, Application of a semi-detailed soot modeling approach for conventional and low temperature diesel combustion – Part I: Model performance, *Fuel* (2015) 757-770.
37. G. D'Errico, T. Lucchini, F. Contino, M. Jangi, X.-S. Bai, Comparison of well-mixed and multiple representative interactive flamelet approaches for diesel spray combustion modelling, *Combust. Theor. Model.* 18 (2013) 65-88.
38. C. Gong, M. Jangi, X.-S. Bai, Diesel flame lift-off stabilization in the presence of laser-ignition: a numerical study, *Combust. Theor. Model.* 19 (2015) 696-713,
39. S. Gallot-Lavallée, W.P. Jones, Large Eddy Simulation of spray auto-ignition under EGR conditions, *Flow Turb. Combust.* 96 (2016) 513-534.
40. S.S. Pandurangi, M. Bolla, Y.M. Wright, K. Boulouchos, S.A. Skeen, J. Manin, Onset and progression of soot in high-pressure *n*-dodecane sprays under diesel engine conditions, *Int. J. Eng. Res.*, doi:10.1177/1468087416661041.
41. A. Wehrfritz, O. Kaario, V. Vuorinen, B. Somers, Large Eddy Simulation of *n*-dodecane spray flames using Flamelet Generated Manifolds, *Combust. Flame* 167 (2016) 113-131.

42. M. Jangi, T. Lucchini, G. D'Errico, X.S. Bai, Effects of EGR on the structure and emissions of diesel combustion, *Proc. Comb. Inst.* 34 (2013) 3091-3098.
43. K.M. Pang, H.M. Poon, H.K. Ng, S. Gan, J. Schramm, Soot formation modeling of *n*-dodecane and diesel sprays under engine-like conditions. SAE paper 2015-24-2468; 2015.
44. M. Bolla, M.A Chishty, E.R. Hawkes, S. Kook, Modeling combustion under engine combustion network Spray A conditions with multiple injections using the transported probability density function method, *Int. J. Engine Research* 18 (2017) 6–14.
45. M. Bolla, M.A Chishty, E.R. Hawkes, N.Q. Chan, S. Kook, Influence of turbulent fluctuations on radiation heat transfer, NO and soot formation under ECN Spray A conditions, *Proc. Comb. Inst.* 36 (2017) 3551-3558.
46. S. Amzin, N. Swaminathan, J.W. Rogerson, J.H. Kent, Conditional Moment Closure for turbulent premixed flames, *Combust. Sci. Tech.* 184 (2012) 1743-1767.
47. De Paola G. De Paola , E. Mastorakos , Y.M. Wright, K. Boulouchos, Diesel engine simulations with multi-dimensional conditional moment closure, *Combust. Sci. Tech.* 180 (2008) 883-899.
48. S.-C. Kong, Y. Sun, R.D. Reitz, Modeling diesel spray flame lift-off, sooting tendency, and NO<sub>x</sub> emissions using detailed chemistry with phenomenological soot model, *ASME J. Eng. Gas Turb. Power* 129 (2007) 245-251.
49. D.C. Haworth, Progress in probability density function methods for turbulent reacting flows, *Prog. Energy Combust. Sci.* 36 (2010) 168-259.
50. L. Valino, A field Monte Carlo formulation for calculating the probability density function of a single scalar in a turbulent flow, *Flow Turbul. Combust.* 60 (1998) 157-172.
51. J. Jaishree, D. C. Haworth, Comparisons of Lagrangian and Eulerian PDF methods in simulations of non-premixed turbulent jet flames with moderate-to-strong turbulence-chemistry interactions, *Combust. Theor. Model.* 16 (2012) 435-463.
52. The OpenFOAM Foundation. 2015. Available at [www.openfoam.org/](http://www.openfoam.org/).

53. R. Lin, L.L. Tavlarides, Thermophysical properties needed for the development of the supercritical diesel combustion technology: Evaluation of diesel fuel surrogate models, *J. Supercrit. Fluids* 71 (2012) 71:136-146.
54. W.P. Jones, A.J. Marquis, V.N. Prasad, LES of a turbulent premixed swirl burner using the Eulerian stochastic field method, *Combust. Flame* 159 (2012) 3079-3095.
55. M. Jangi, X.-S. Bai, Multidimensional chemistry coordinate mapping approach for combustion modeling with finite-rate chemistry, *Combust. Theory Model.* 16 (2012) 1109-1132.
56. M. Jangi, X. Zhao, D.C. Haworth, X.S. Bai, Stabilization and lift-off length of a non-premixed methane/air jet flame discharging into a high-temperature environment: An accelerated transported PDF method, *Combust. Flame* 162 (2015) 408-419.
57. E. Hodzic, M. Jangi, R.Z. Szasz, X.S. Bai, Large eddy simulation of bluff body flames close to blow-off using an Eulerian stochastic field method, *Combust. Flame* 181 (2017) 1-15.
58. M. Jangi, M. Altarawneh, B.Z. Dlugogorski, Large-eddy simulation of methanol pool fires using an accelerated stochastic fields method, *Combust. Flame* 173 (2017) 89-98.
59. L. Liang, J. G. Stevens, J. T. Farrell, A dynamic multi-zone partitioning scheme for solving detailed chemical kinetics in reactive flow computations, *Combust. Sci. Technology* 181 (2009) 1345-1371.
60. G. M. Goldin, Z. Ren, S. Zahirovic, A cell agglomeration algorithm for accelerating detailed chemistry in CFD, *Combust. Theor. Model.* 4 (2009) 721-739.
61. T. Yao, Y. Pei, B. Zhong, S. Som, T. Lu, A hybrid mechanism for n-dodecane combustion with optimized low-temperature chemistry, 9<sup>th</sup> U.S. National Combustion Meeting, 114IC-0055, May 17-20, 2015, Cincinnati, OH, US.
62. V.I. Golovitchev, M. Bergman, L. Montorsi, CFD Modeling of diesel oil and DME performance in a two-stroke free piston engine, *Combust. Sci. Tech.* 179 (2007) 417-436.

63. Y. Ra, R.D. Reitz, A combustion model for IC engine combustion simulation with multi-component fuels, *Combust. Flame* 158 (2011) 69-90.
64. E. Ranzi, A. Frassoldati, A. Stagni, M. Pelucchi, A. Cuoci, T. Faravelli, Reduced kinetic schemes of complex reaction systems: fossil and biomass-derived transportation fuels, *Int. J. Chem. Kinet.* 46 (2014) 512-542.
65. A. Patel, S.C. Kong SC, R.D. Reitz, Development and validation of a reduced reaction mechanism for HCCI engine simulations. SAE paper 2004-01-0558; 2004.
66. S. Liu, J.C. Hewson, J.H. Chen, H. Pitsch, Effects of strain rate on high-pressure nonpremixed *n*-heptane autoignition in counterflow, *Combust Flame* 137 (2004) 320-339.
67. T. Lu, C.K. Law, Strategies for mechanism reduction for large hydrocarbon: *n*-heptane, *Combust. Flame* 154 (2008) 153-163.
68. T. Lucchini, G. D'Errico, D. Ettorre, Numerical investigation of the spray-mesh-turbulence interactions for high-pressure, evaporating sprays at engine conditions, *Int. J. Heat Fluid Flow* 32 (2011) 285-297.
69. V. Raman, R.O. Fox, A.D. Harvey, Hybrid finite-volume/transported PDF simulations of a partially premixed methane-air flame, *Combust. Flame* 124 (2004) 327-350.
70. R.R. Cao, S.B. Pope, A.R. Masri, Turbulent lifted flames in a vitiated coflow investigated using joint PDF calculations, *Combust. Flame* 142 (2005) 438-453.
71. J.D. Blouch, J.-Y. Chen, C.K. Law, A joint scalar PDF study of nonpremixed hydrogen ignition, *Combust. Flame* 135 (2003) 209-225.
72. R.R. Cao, H. Wang, S.B. Pope, The effect of mixing models in PDF calculations of piloted jet flames, *Proc. Combust. Inst.* 31 (2007) 1543-1550.
73. E. H. Kung and D. C. Haworth, Transported Probability Density Function (tPDF) Modeling for Direct-Injection Internal Combustion Engines, SAE 2008-01-0969, 2008.

74. O.H. Nielsen, Niflheim Linux supercomputer cluster. Available at  
<https://wiki.fysik.dtu.dk/niflheim/> [accessed on 26 August 2017].
75. Y. Mizobuchi, S. Tachibana, J. Shinio, S. Ogawa, T. Takeno, A numerical analysis of the structure of a turbulent hydrogen jet lifted flame, *Proc. Combust. Inst.* 29 (2002) 2009-2015.
76. A.J. Lock, A.M. Briones, X. Qin, S.K. Aggarwal, I.K. Puri, U. Hegde, Lift-off characteristics of partially premixed flames under normal and microgravity conditions, *Combust Flame* 143 (2005) 159-173.
77. A.M. Briones, S.K. Aggarwal, V.R. Katta, Effects of H<sub>2</sub> enrichment on the propagation characteristics of CH<sub>4</sub>-air triple flames, *Combust. Flame* 153 (2008) 367-383.
78. F. Zhang, R. Yu, X.S. Bai, Effect of split fuel injection on heat release and pollutant emissions in partially premixed combustion of PRF70/air/EGR mixtures, *Appl. Energy* 149 (2015) 283-296.
79. S.R. Turns, *An introduction to combustion: concepts and applications* (3<sup>rd</sup> ed.) McGraw-Hill International Edition, New York (2012).
80. J.E. Dec, Advanced compression-ignition engines - understanding the in-cylinder process, *Proc. Combust. Inst.* 32 (2009) 2727-2742.
81. A. Joedickea, N. Peters, M. Mansour, The stabilization mechanism and structure of turbulent hydrocarbon lifted flames, *Proc. Combust. Inst.* 30 (2005) 901-909.
82. J. Pragera, H.N. Najma, M. Valoranib, D.A. Goussisc, Structure of *n*-heptane/air triple flames in partially-premixed mixing layers, *Combust. Flame* 158 (2011) 2128-2144.
83. K.K. Kuo, *Principle of combustion* (2<sup>nd</sup> ed.) John Wiley & Sons, New Jersey (2005).
84. R.L. Gordon, A.R. Masri, S.B. Pope, G.M. Goldin, Transport budgets in turbulent lifted flames of methane autoigniting in a vitiated co-flow, *Combust. Flame* 151 (2007) 495-511.

## Appendix A

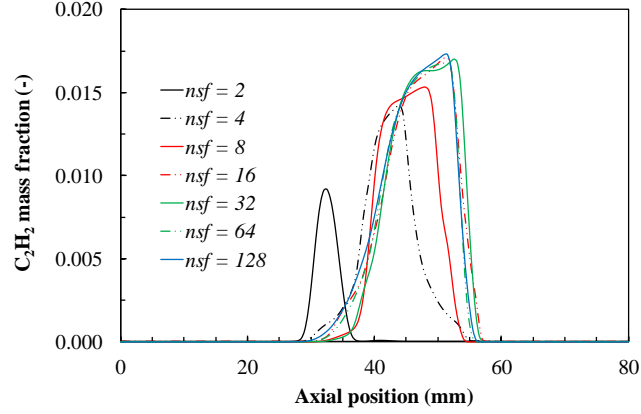


Fig. A1. Comparison of acetylene ( $C_2H_2$ ) profiles using different number of stochastic fields along the spray axis.

## Appendix B

### Calculations of the equivalence ratio when the mass fractions of the air/EGR mixture are known

The local equivalence ratio,  $\phi$  is defined as

$$\phi = (Y_F/Y_{O_2}) / (F/O)_{st} \quad (1)$$

The mass fraction of material that is originated from the fuel is

$$Y_F = Y_{C,F} + Y_{H,F} + Y_{O,F} \quad (2)$$

In combustion, the elements are conserved and this the carbon, hydrogen and oxygen element mass fraction in the products are the same as those before the reaction. However, the carbon, hydrogen and oxygen elements from the EGR need to be taken into account when determining the local equivalence ratio. We know the C and H element mass fractions from the EGR. They are denoted  $Y_{C,E}$  and  $Y_{H,E}$  respectively.

$$Y_{C,F} + Y_{C,E} = Y_{C,P}$$

$$Y_{C,F} = Y_{C,P} - Y_{C,E} \quad (3)$$

$$Y_{H,F} + Y_{H,E} = Y_{H,P}$$

$$Y_{H,F} = Y_{H,P} - Y_{H,E} \quad (4)$$

$$Y_{O,F} + Y_{O,A} + Y_{O,E} = Y_{O,P} \quad (5)$$

Assume that the element mass ratio of O to H in the fuel is  $\theta$ ,

$$Y_{O,F} = \theta Y_{H,F}$$

$$= \theta (Y_{H,P} - Y_{H,E}) \quad (6)$$

Substitute Eqs. (3), (4) and (6) into Eq. (2), we get

$$Y_F = Y_{C,P} - Y_{C,E} + Y_{H,P} - Y_{H,E} + \theta (Y_{H,P} - Y_{H,E}) \quad (7)$$

The mass fraction of material that is originated from the oxygen is

$$Y_{O2} = Y_{O2,A} + Y_{O2,E} \quad (8)$$

For Eq. (5), the total mass fraction of O element in the air is originated from oxygen,

$$Y_{O,A} = Y_{O2,A} \quad (9)$$

while the total mass fraction of O element in EGR come from  $O_2$ ,  $CO_2$  and  $H_2O$

$$Y_{O,E} = Y_{O2,E} + Y_{O,CO2,E} + Y_{O,H2O,E} \quad (10)$$

Based on Eqs. (6), (9) and (10), Eq. (5) can be re-written as

$$Y_{O2,A} + Y_{O2,E} = Y_{O,P} - Y_{O,CO2,E} - Y_{O,H2O,E} - \theta (Y_{H,P} - Y_{H,E}) \quad (11)$$

Substitute Eqs. (7) and (11) into Eq. (1), the local equivalence ratio is

$$\phi = [(Y_{C,P} - Y_{C,E} + Y_{H,P} - Y_{H,E} + \theta (Y_{H,P} - Y_{H,E})) / \{ [Y_{O,P} - Y_{O,CO2,E} - Y_{O,H2O,E} - \theta (Y_{H,P} - Y_{H,E})](F/O)_{st} \}] \quad (12)$$

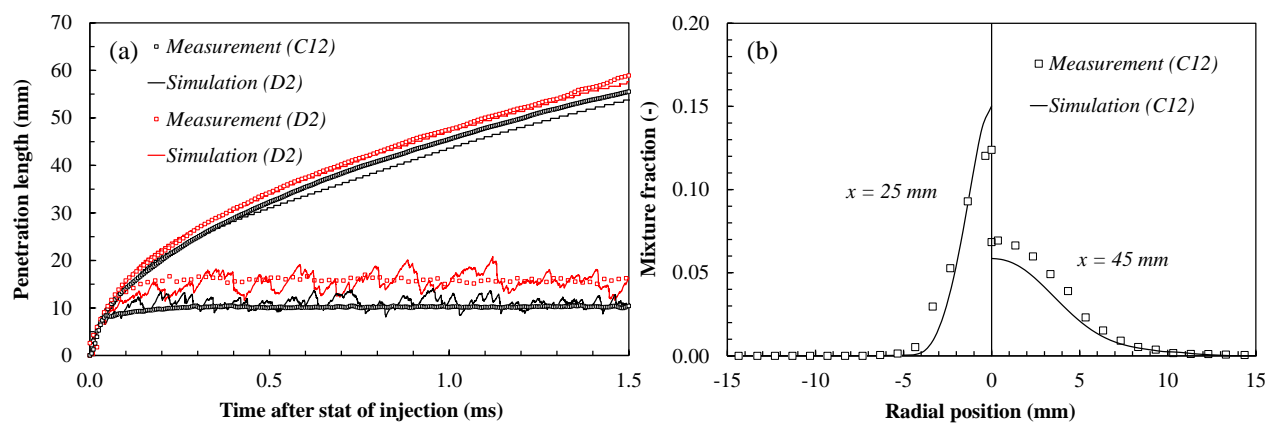


Fig. 1. Comparisons of measurements [4,6] to (a) penetration lengths simulated for diesel (D2) and  $n$ -dodecane ( $C_{12}$ ) fuels as well as (b) mixture fraction profiles of non-reacting  $n$ -dodecane ( $C_{12}$ ) spray at quasi-steady state for different positions.

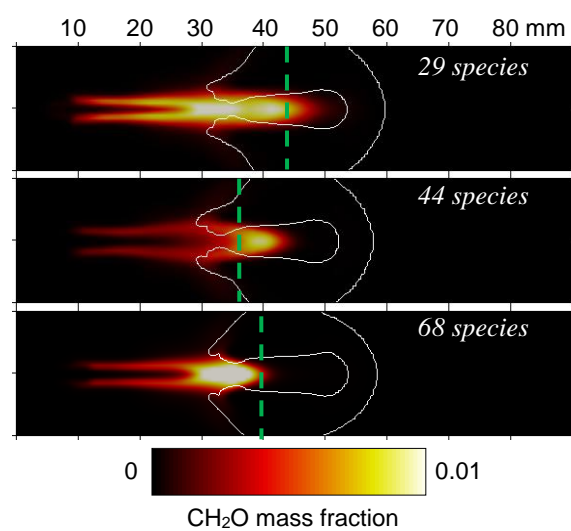


Fig. 2. Comparisons of  $\text{CH}_2\text{O}$  distribution and OH iso-contour (white solid lines) simulated using different chemical kinetic mechanisms. The green dotted lines indicate the flame lift-off positions generated using the WSR model.

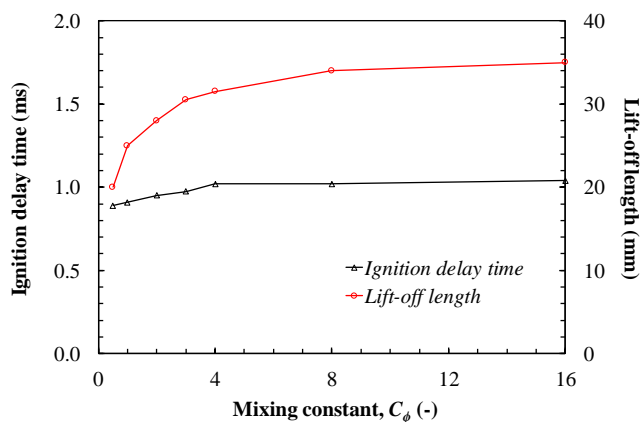


Fig. 3. Comparisons of ignition delay time and lift-off length simulated using different mixing constants.

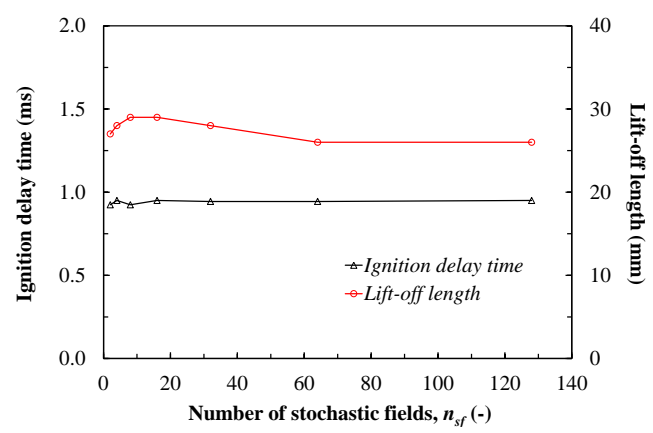


Fig. 4. Comparisons of ignition delay time and lift-off length simulated using different number of stochastic fields.

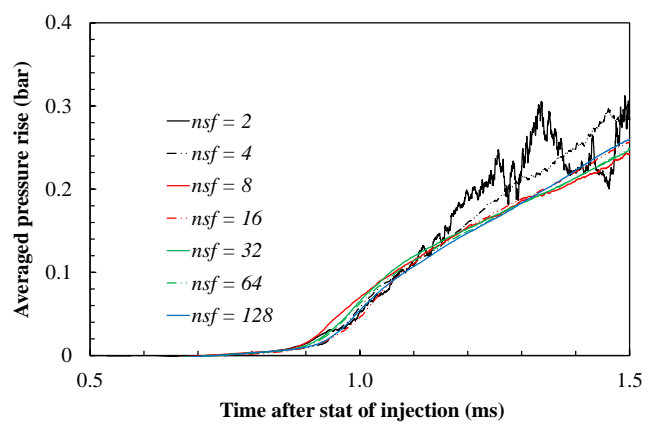


Fig. 5. Comparisons of averaged pressure rise simulated using different number of stochastic fields.

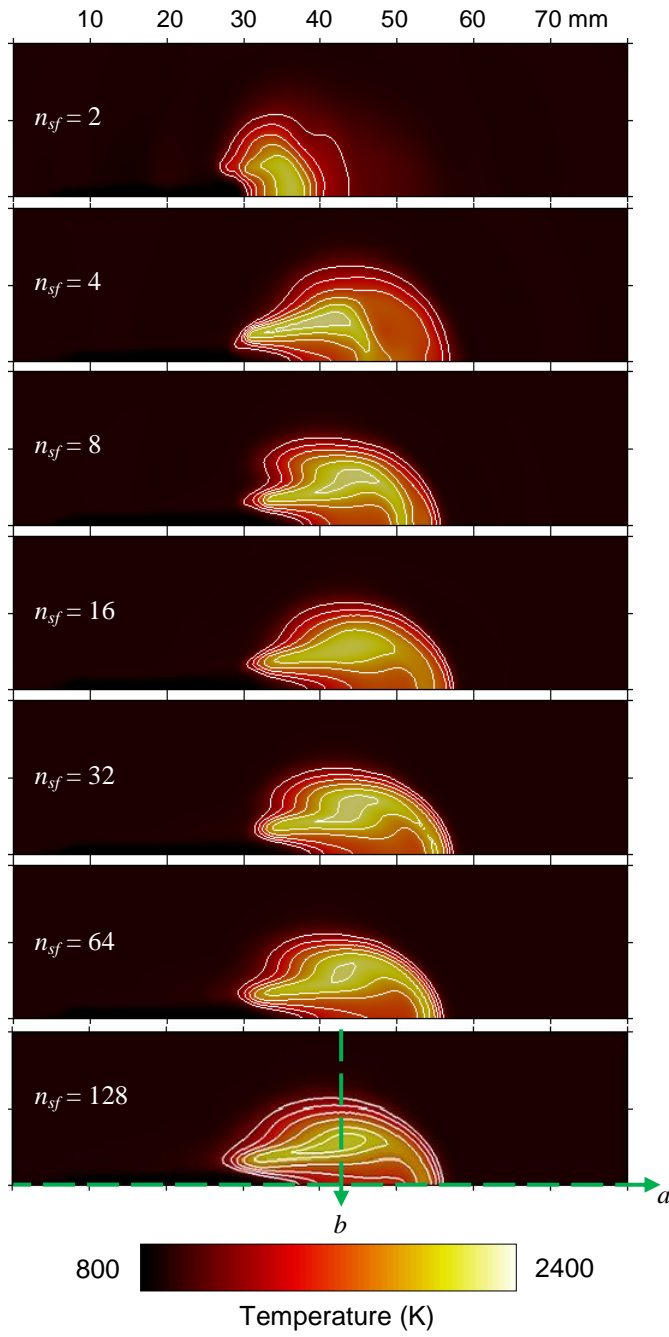


Fig. 6. Comparisons of temperature distributions using different number of stochastic fields. Temperature and mass fractions of various combustion products along the spray axis (a) and downstream across the diffusion flame (b) computed using different numbers of stochastic fields are compared.

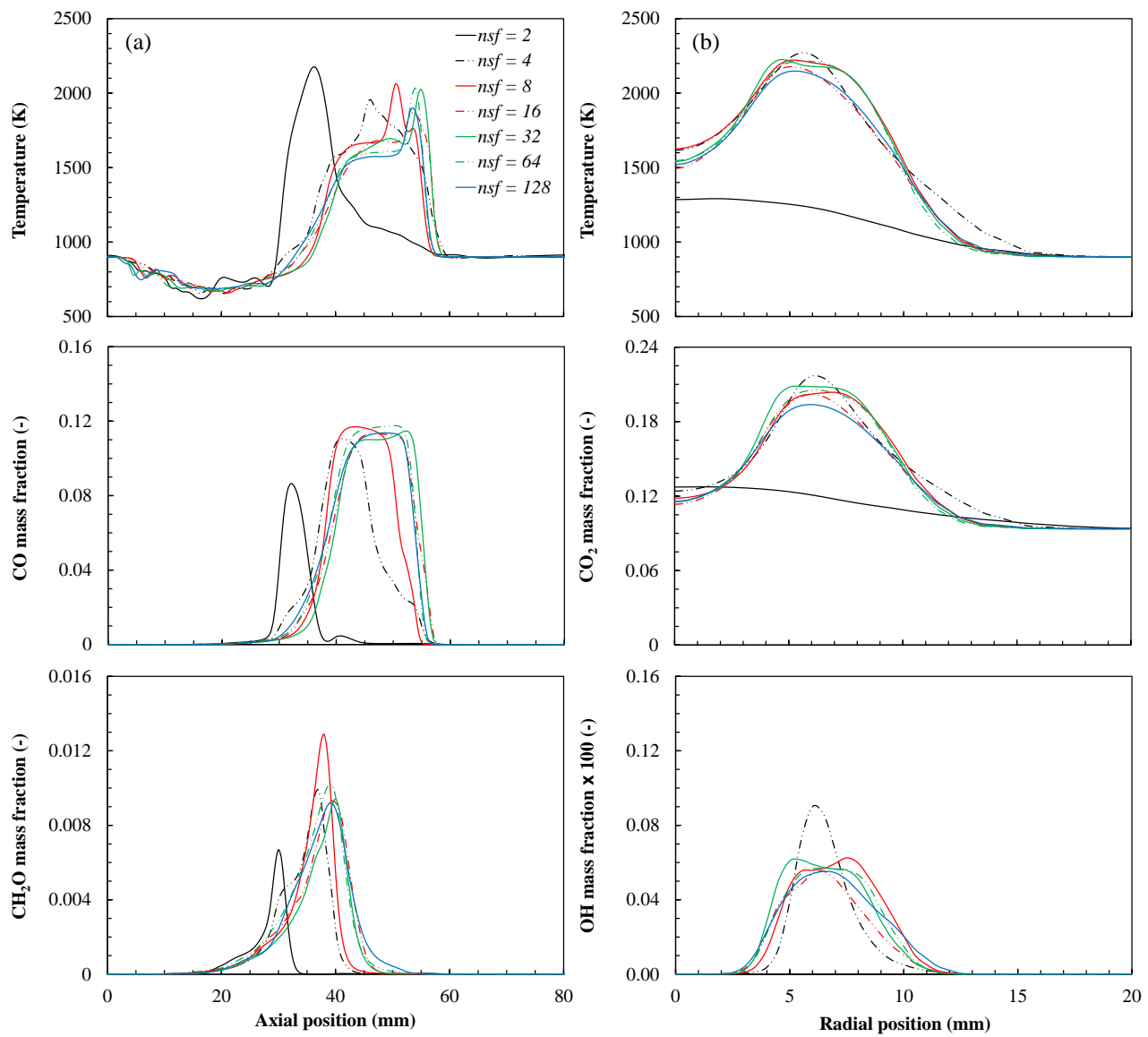


Fig. 7. Comparisons of temperature and combustion product profiles using different number of stochastic fields (a) along the spray axis and (b) downstream across the diffusion flame.

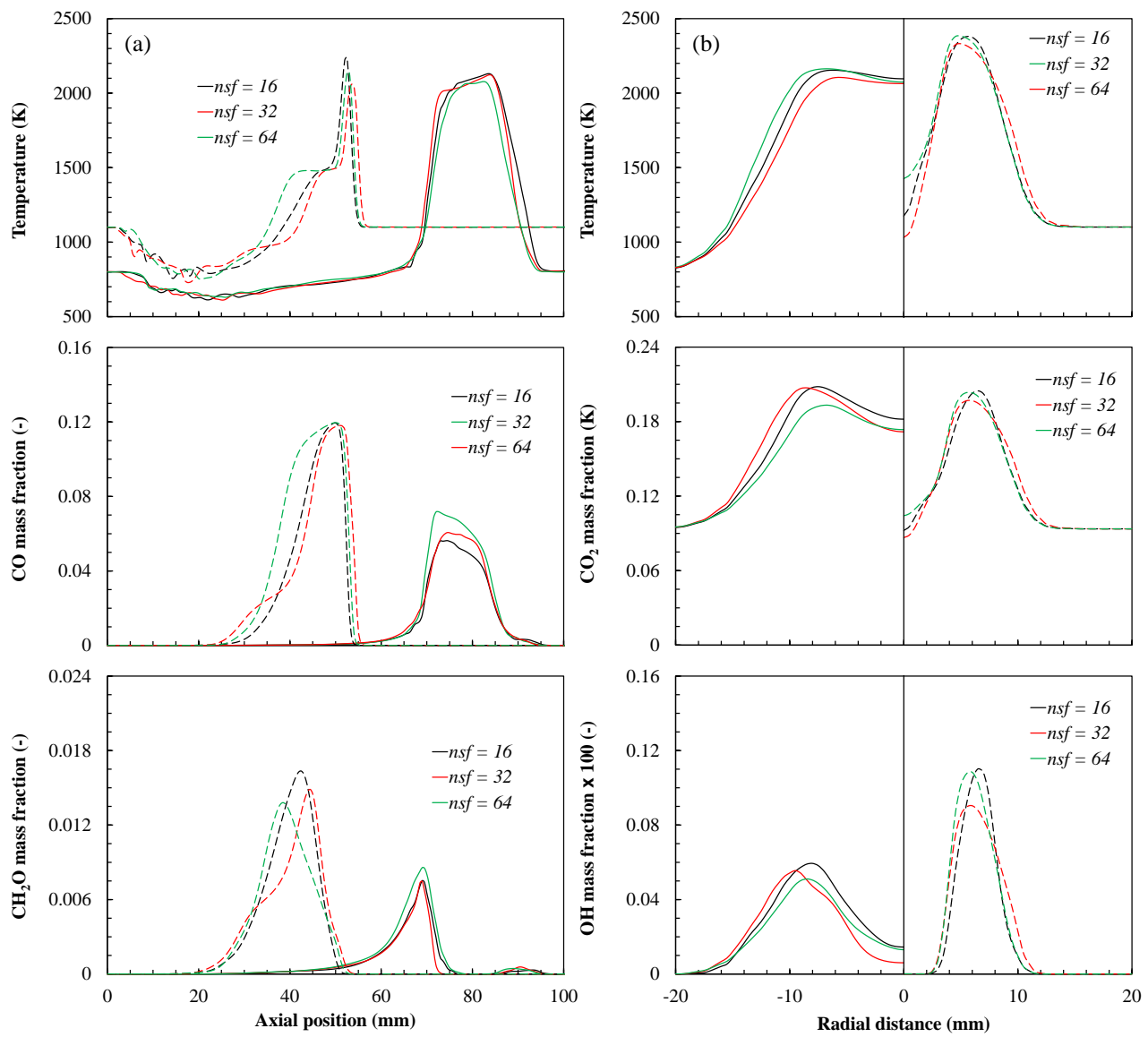


Fig. 8. Comparisons of temperature and combustion product profiles using different number of stochastic fields (a) along the spray axis and (b) downstream across the diffusion flame for the 800 K; 15% O<sub>2</sub> case (solid line) and the 1100 K; 15% O<sub>2</sub> case (dotted line).

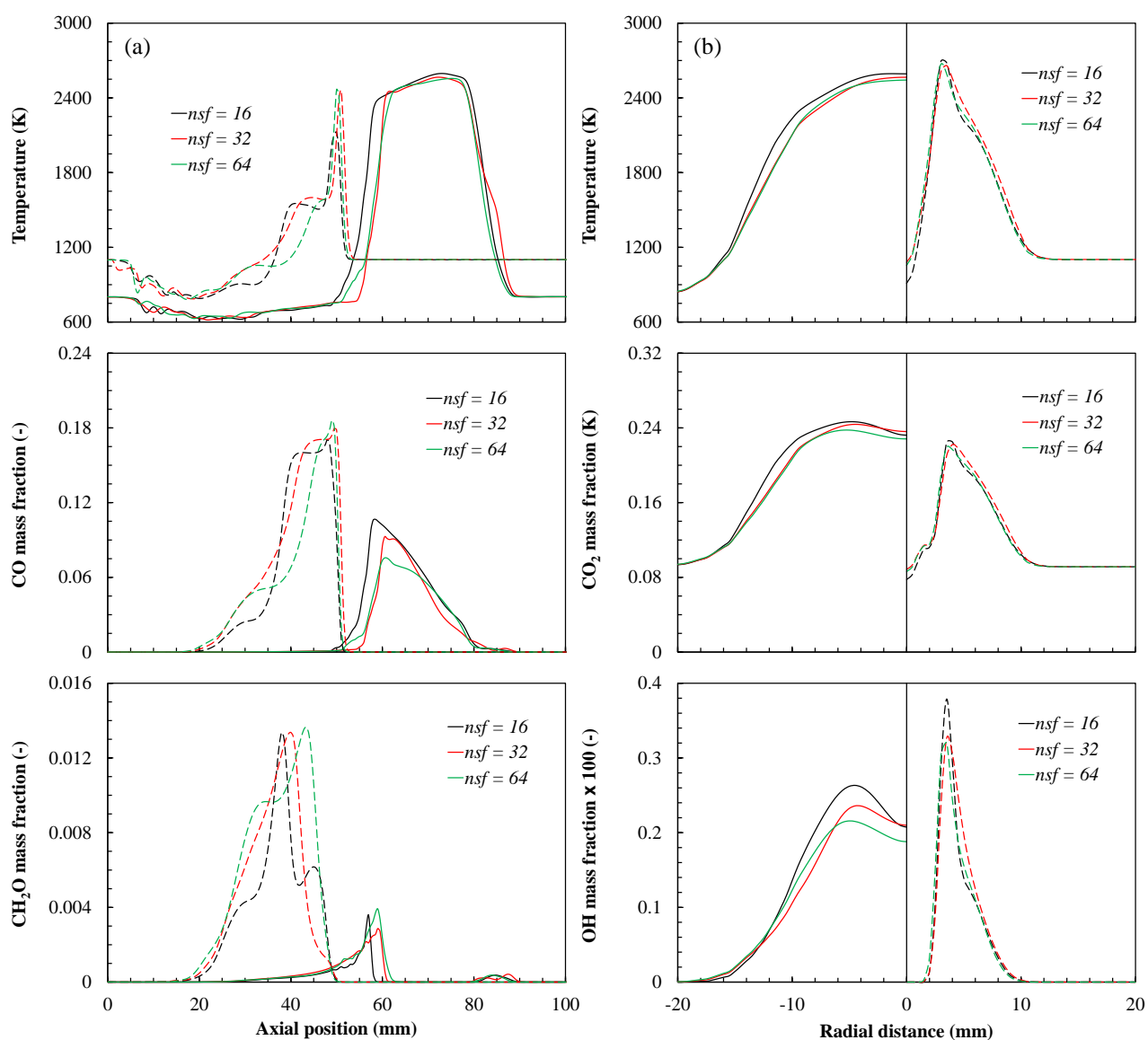


Fig. 9. Comparisons of temperature and combustion product profiles using different number of stochastic fields (a) along the spray axis and (b) downstream across the diffusion flame for the 800 K; 21% O<sub>2</sub> case (solid line) and the 1100 K; 21% O<sub>2</sub> case (dotted line).

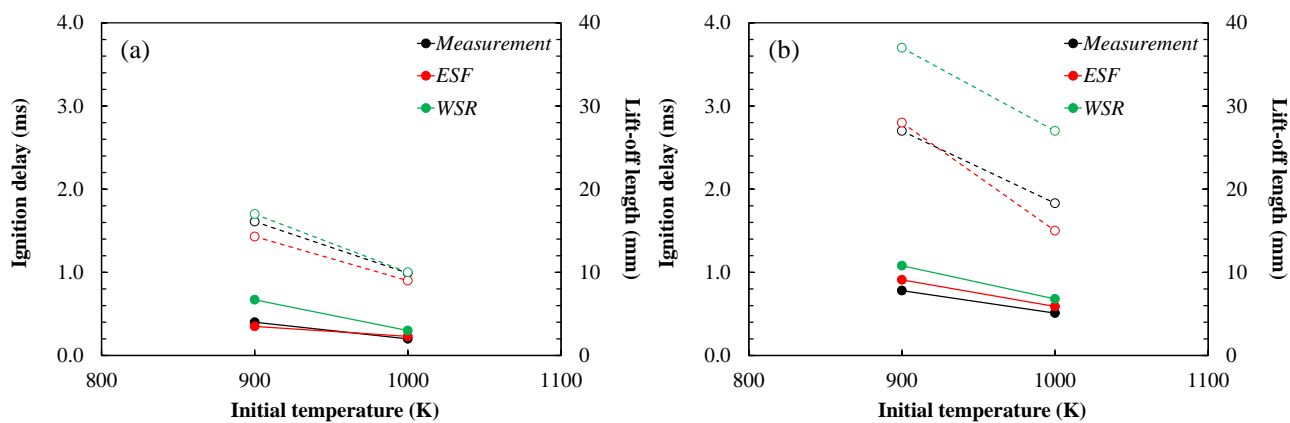


Fig. 10. Comparisons of simulated ignition delay times (solid lines) and lift-off lengths (dotted lines) to the measurements [4,6] for (a) *n*-dodecane and (b) D2 fuels. The simulations are performed at ambient temperatures of 900 K and 1000 K for ambient O<sub>2</sub> of 15% and ambient density of 22.8 kg/m<sup>3</sup> (cases 3 to 6).

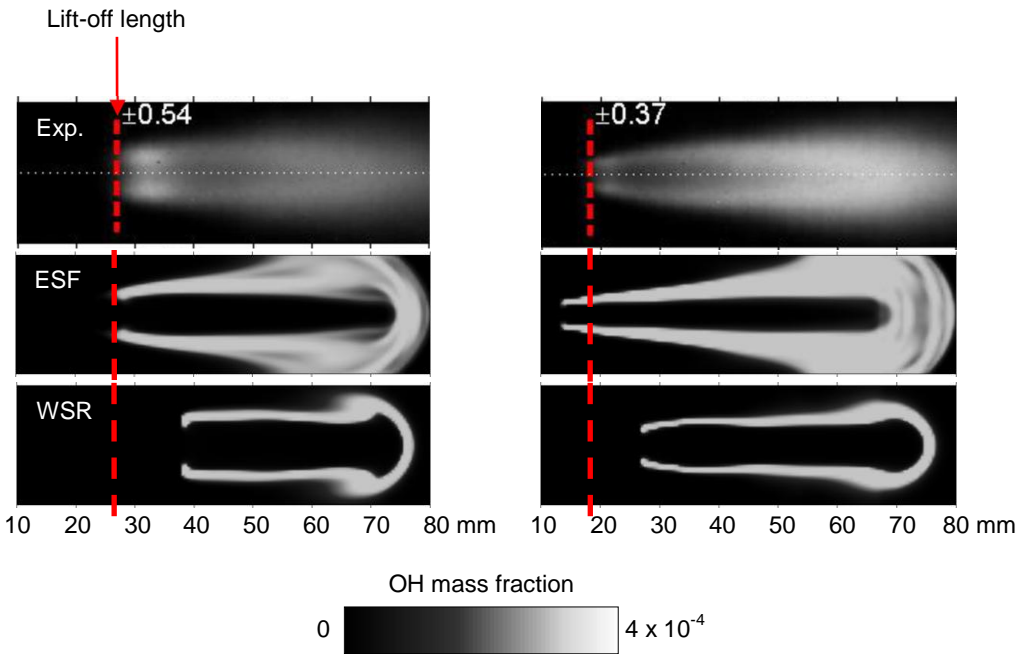


Fig. 11. Comparisons of simulated flame lift-offs and OH distributions using the ESF and WSR models to the measurements [5] at the ambient temperatures of 900 K (left) and 1000 K (right). The red dotted lines in Fig. 11 represent the experimental lift-off lengths in their respective case.

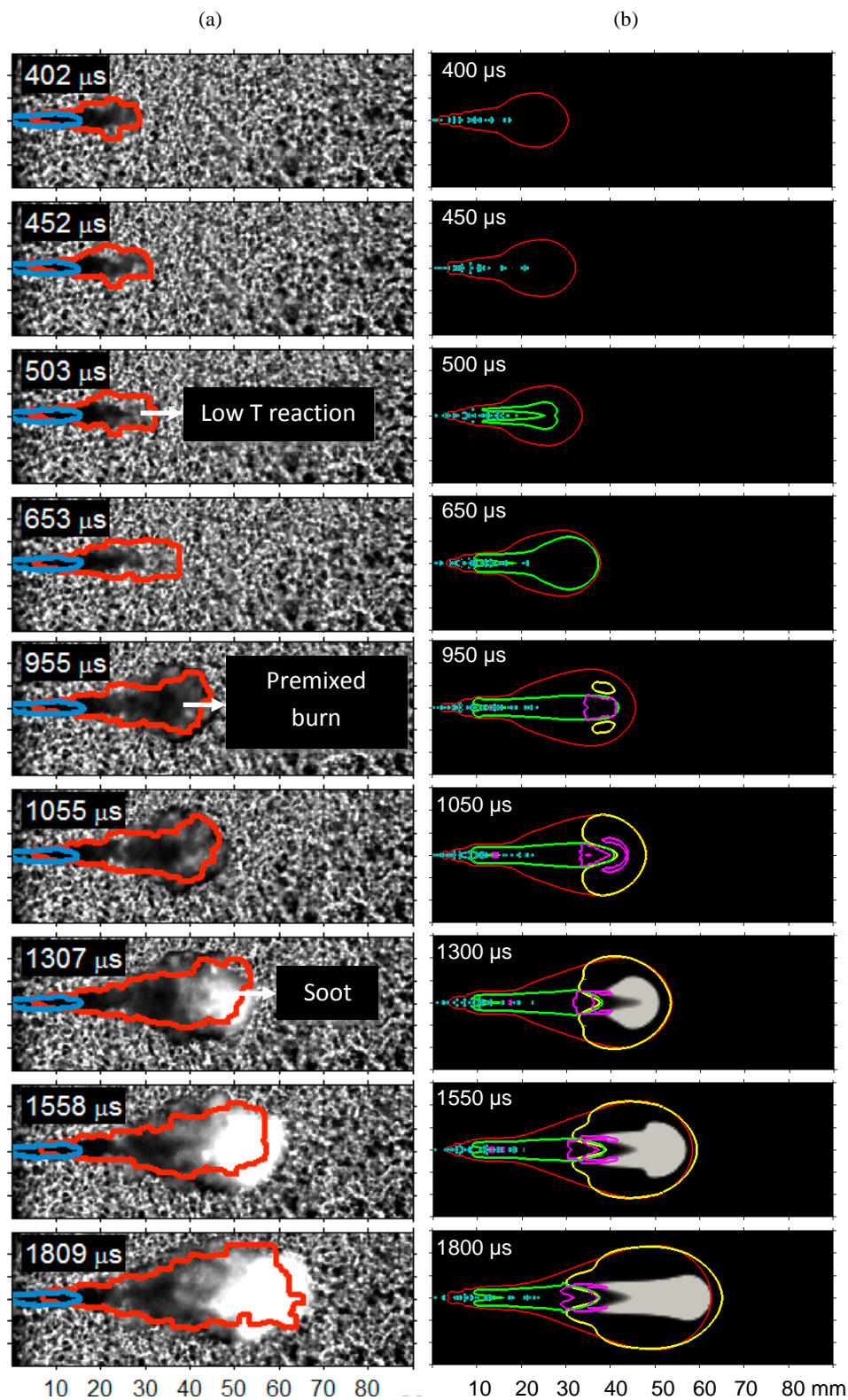


Fig. 12. (a) Spray, flame and soot developments recorded from the experiment and (b) the simulated soot volume fraction contour with iso-contours for fuel vapour (red),  $C_7H_{15}O_2$  mass fraction (green), rich premixed flame (purple) and temperature (yellow).

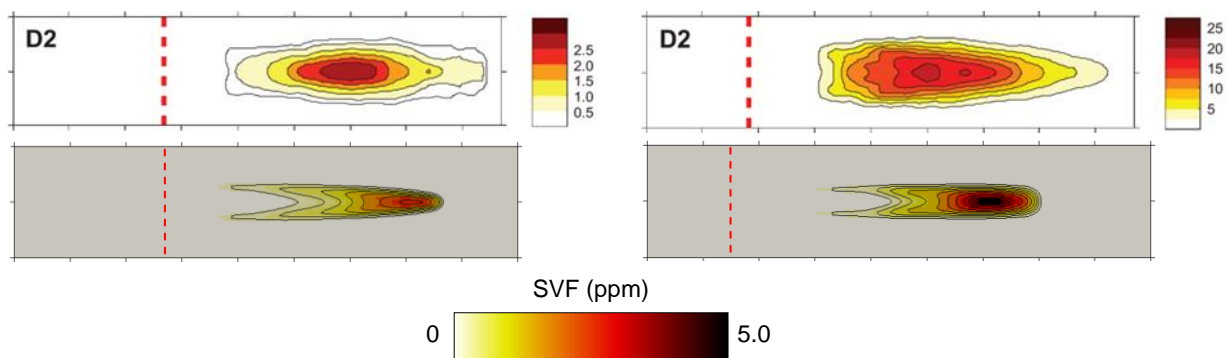


Fig. 13. Comparisons of simulated soot distributions using the ESF models (bottom) to the measurements [5] (top) at the ambient temperatures of 900 K (left) and 1000 K (right). Each iso-contour (black lines) of the simulation results represents a soot volume fraction interval of 0.5 ppm.

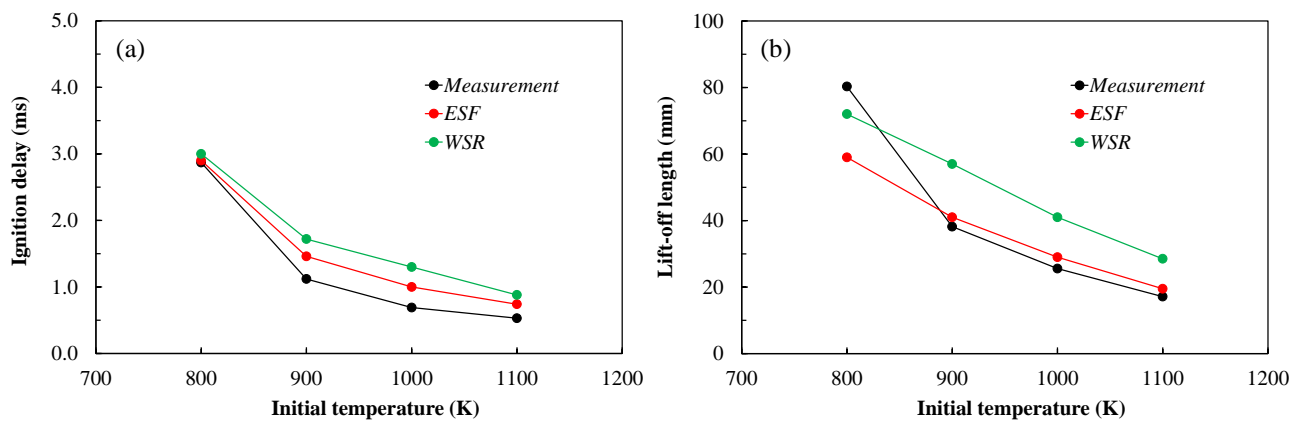


Fig. 14. Comparisons of simulated (a) ignition delay times and (b) lift-off lengths to the measurements [3] for ambient temperatures ranging from 800 K to 1100 K at ambient  $O_2$  of 15% and ambient density of  $14.8 \text{ kg/m}^3$ .

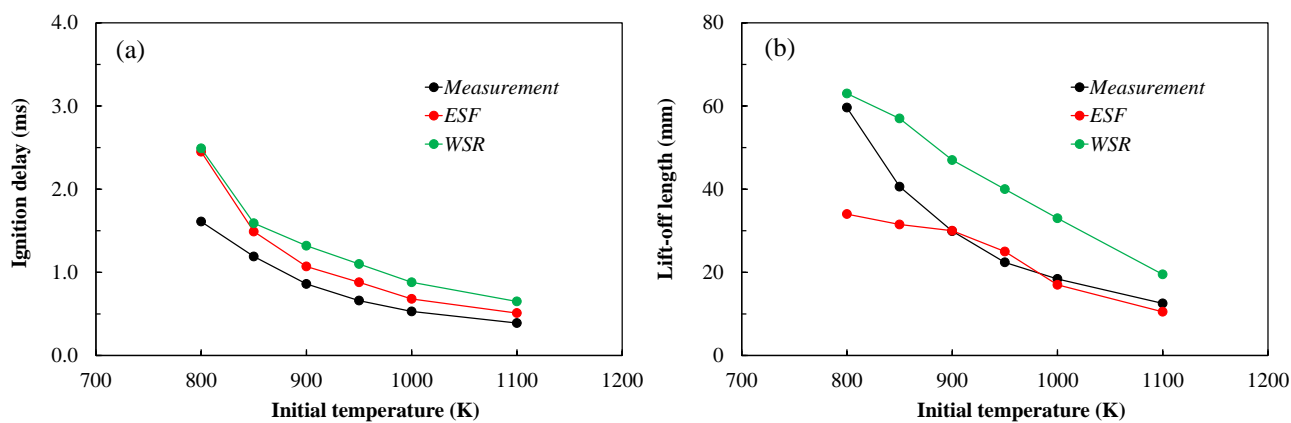


Fig. 15. Comparisons of simulated (a) ignition delay times and (b) lift-off lengths to the measurements [3] for ambient temperatures ranging from 800 K to 1100 K at ambient  $O_2$  of 21% and ambient density of  $14.8 \text{ kg/m}^3$ .

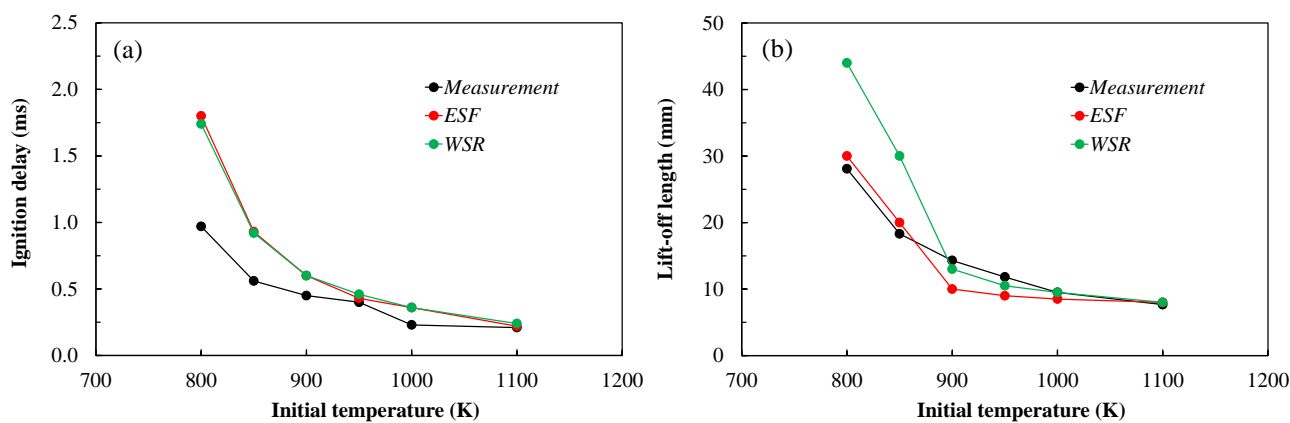


Fig. 16. Comparisons of simulated (a) ignition delay times and (b) lift-off lengths to the measurements [3] for ambient temperatures ranging from 800 K to 1100 K at ambient  $O_2$  of 21% and ambient density of  $30.0 \text{ kg/m}^3$ .

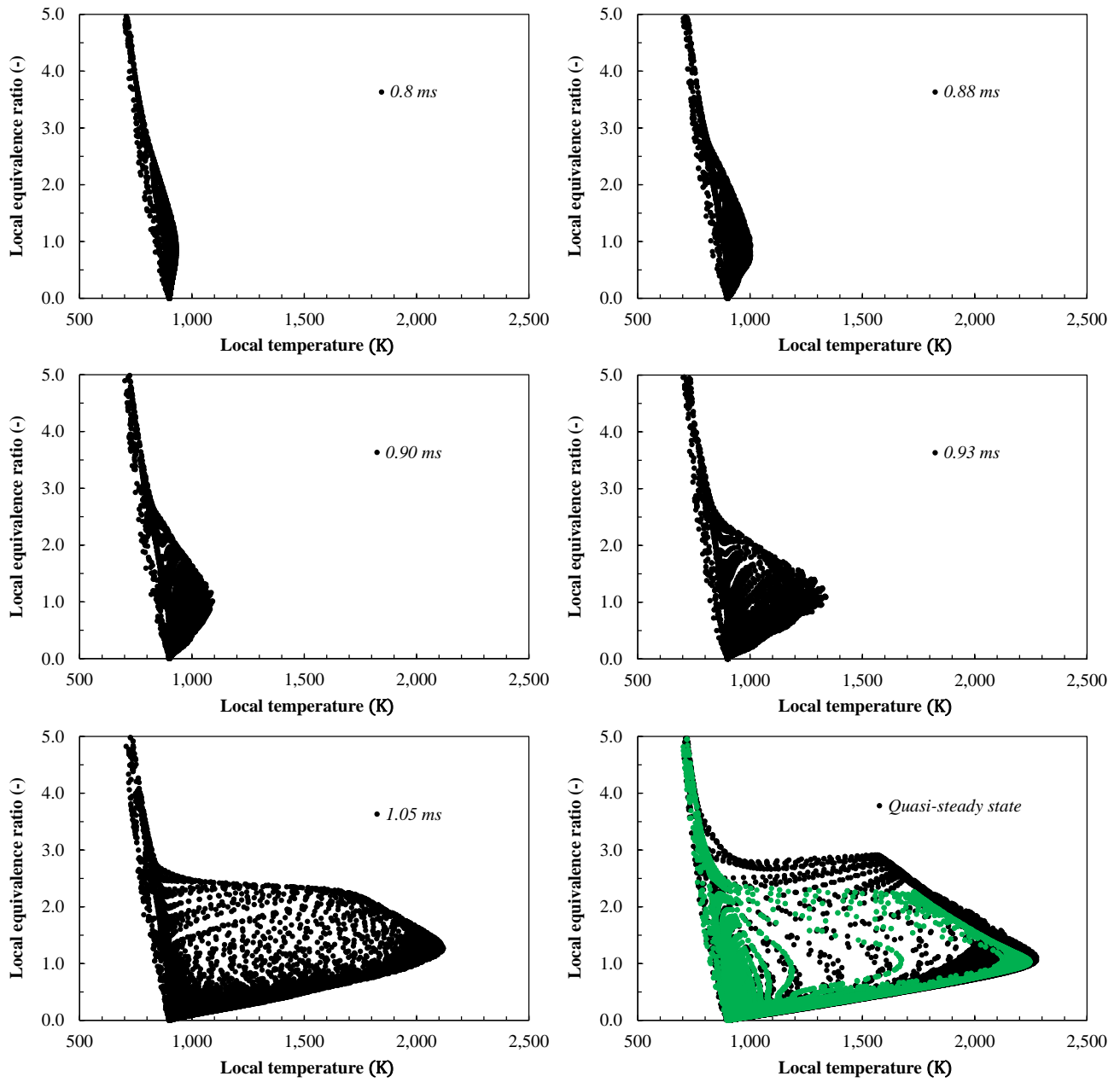


Fig. 17. Evolution of the temperature-equivalence ratio characteristics from low-temperature reaction to quasi-steady state. The black and green dots represent the ESF and WSR results respectively.

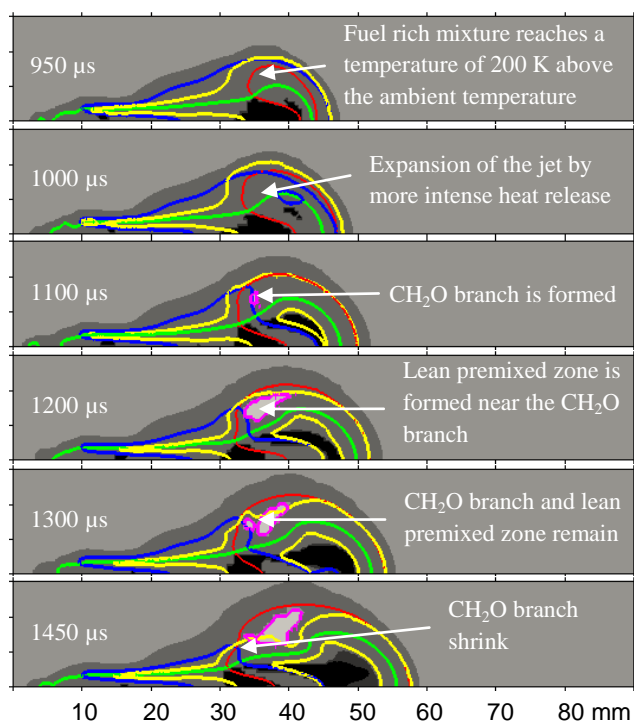


Fig. 18. Transient developments of flame structures computed using the ESF model for the  $22 \text{ kg/m}^3$ ; 900 K; 15%  $\text{O}_2$  condition.

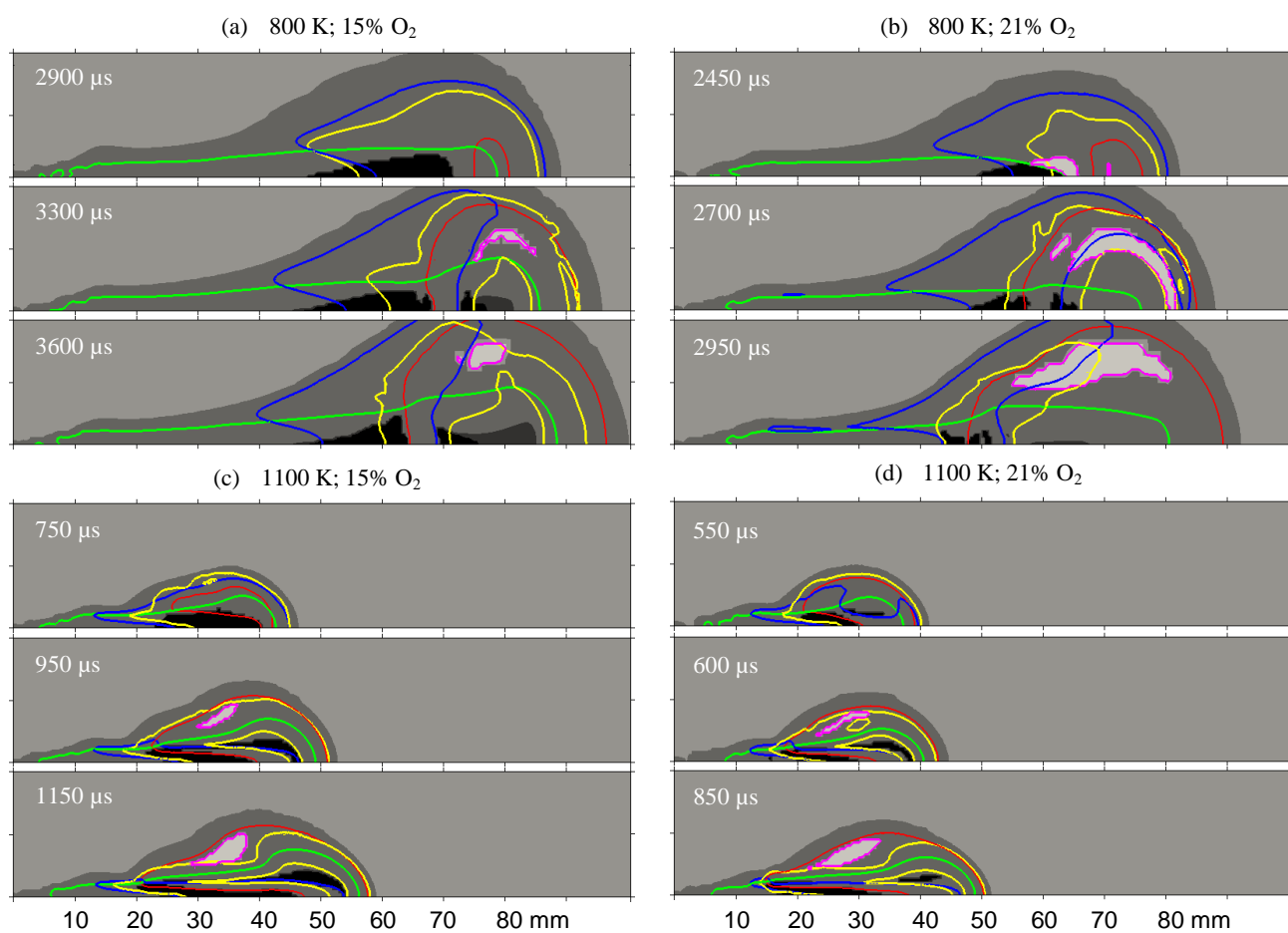


Fig. 19. Transient developments of flame structures computed using the ESF model for (a) 800 K; 15% O<sub>2</sub>, (b) 800 K; 21% O<sub>2</sub>, (c) 1100 K; 15% O<sub>2</sub> and (d) 1100 K; 21% O<sub>2</sub> conditions in the low-pressure cases.

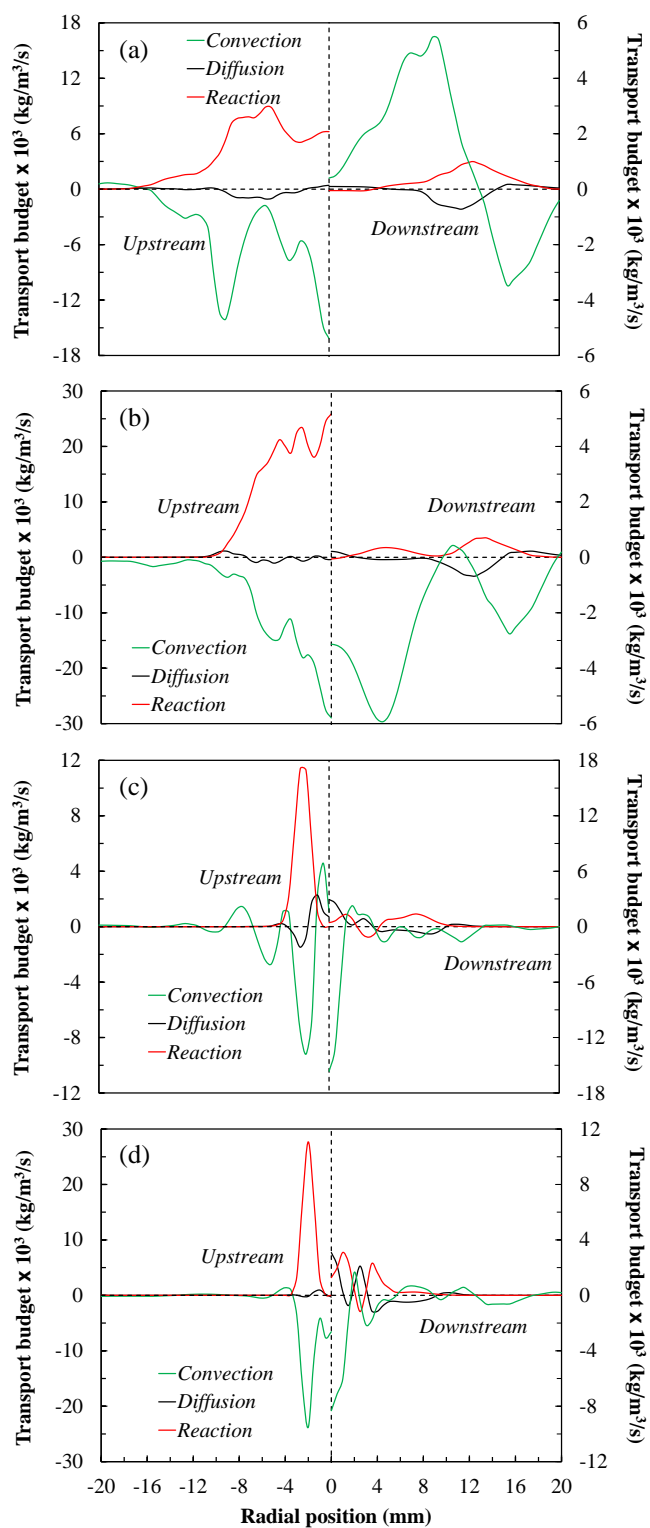


Fig. 20. Comparisons of the convection, diffusion and the reaction terms of  $\text{CO}_2$  for (a) 800 K; 15%  $\text{O}_2$ , (b) 800 K; 21%  $\text{O}_2$ , (c) 1100 K; 15%  $\text{O}_2$ , and (d) 1100 K; 21%  $\text{O}_2$  conditions in the low-pressure cases.